Discrete Element Modeling of Southeast Asia's 3D Lithospheric Deformation During the Indian Collision

Liqing Jiao, Paul Tapponnier, Frédéric-victor Donzé, Luc Scholtes, Yves Gaudemer, Xiwei Xu

JGR Solid Earth

RESEARCH ARTICLE
10.1029/2022JB025578

Discrete Element Modeling of Southeast Asia's 3D Lithospheric Deformation During the Indian Collision

Liqing Jiao[1,2], Paul Tapponnier[3], Frédéric-Victor Donzé[4], Luc Scholtès[5], Yves Gaudemer[6], and Xiwei Xu[3]

[1]SinoProbe Lab, Chinese Academy of Geological Sciences, Beijing, China, [2]Institute of Geology, Chinese Academy of Geological Sciences, Beijing, China, [3]National Institute of Natural Hazards, MEMC, Beijing, China, [4]Université Grenoble Alpes, ISTerre, Grenoble, France, [5]CNRS, IRD, OPGC, Laboratoire Magma et Volcans, Université Clermont Auvergne, Clermont-Ferrand, France, [6]Institute de Physique du Globe, Paris, France

Abstract The Indian collision has deformed the eastern Asian continent in a multifaceted way, uplifting Tibet and surrounding mountains, activating ≥1,000 km-long strike-slip faults, and opening Tertiary rifts and oceanic basins up to ≈3,000 km away from the Himalayas. Modeling such broad-scale tectonics has been challenging. While continent-scale, lithospheric deformation appears to have been primarily taken-up by long, narrow, inter-connected shear-zones with large offsets, the contribution of processes such as channel-flow, collapse, delamination, etc… has remained contentious. Here, based on increasing ^{4}G (Geological, Geophysical, Geochronological, Geodetic) evidence including kinematic and timing constraints on the main mechanisms at play, we use Discrete Element (DE) Modeling to simulate and further understand the evolution of 3D strain across east Asia since the onset of collision, ≈55 Ma ago. The planar, 50 million km^2, 125 km-thick models are scaled for gravity. The approach permits mega-fault generation and evolution without pre-arranged initial settings. The results provide insight into fault birth, propagation and motion, as well as mountain building and plateau growth. They corroborate that continental crustal thickening across Tibet alternated with the extrusion of large blocks that rifted apart in the far field. Remarkably, without changes in boundary conditions or indentation rate, the DE model also vindicates slip reversal along initial strike-slip shear zones.

Plain Language Summary To better understand the Tertiary, three-dimensional tectonics of South-Eastern Asia, mostly a result of the north-eastwards penetration of "rigid" India since ≈55 Ma, we use a Discrete Element Modeling approach. The technique permits the generation and evolution of large faults without initial pre-setting. The model results substantiate the northwards growth of 4/5 Tibet sub-plateaus, atop south-dipping, subducted lithospheric slabs. Two long strike-slip faults, comparable to the Ailao-Shan-Red River and Altyn Tagh-Haiyuan shear zones, successively propagate to the eastern boundary of the model, where they generate extensional basins similar to the South China Sea and North China Rifts. They isolate two stable blocks (≈Sunda and South China). Remarkably, without changes in indentation rate, the activation of the northern shear zone triggers slip reversal on the southern one, as observed along Yunnan's Red River faults since the Miocene. On the west side of Sunda, the model generates faults comparable to the Sagaing fault and triangular basins similar to the Andaman and Mergui basins. Finally, the model suggests that crustal thickening across Tibet alternated with strike-slip faulting. The main discrepancy between tectonic observations and model results is the striking difference in strike-slip fault orientation, likely due to age-dependent lithospheric strength.

Key Points:

- Stepwise continental subduction and northward rise of Tibetan mountain ranges, and isolation of intervening captive basins
- Birth and propagation of lithospheric continental shear zones, coupled with far-field opening of rifts and Oceanic basins
- Continental block extrusion and broad-scale fault-slip reversal

Supporting Information:

Supporting Information may be found in the online version of this article.

Correspondence to:

L. Jiao,
jiaoliqing@gmail.com

Citation:

Jiao, L., Tapponnier, P., Donzé, F.-V., Scholtès, L., Gaudemer, Y., & Xu, X. (2023). Discrete Element Modeling of Southeast Asia's 3D lithospheric deformation during the Indian collision. *Journal of Geophysical Research: Solid Earth*, *128*, e2022JB025578. https://doi.org/10.1029/2022JB025578

Received 9 SEP 2022
Accepted 16 DEC 2022

Author Contributions:

Conceptualization: Liqing Jiao, Paul Tapponnier
Data curation: Frédéric-Victor Donzé
Formal analysis: Liqing Jiao, Yves Gaudemer
Funding acquisition: Xiwei Xu
Investigation: Liqing Jiao, Paul Tapponnier
Methodology: Liqing Jiao, Frédéric-Victor Donzé, Luc Scholtès
Resources: Liqing Jiao
Software: Liqing Jiao, Frédéric-Victor Donzé, Luc Scholtès
Supervision: Paul Tapponnier

1. Introduction

The long-lasting convergence between India and Asia, whose present-day rate is ≈40 mm/yr, continues to deform the Asian continent, and has activated all types of faults since the beginning of the Eocene (≈55 Ma) (Figures 1–3). The resulting, broad-scale collisional shortening keeps uplifting the Himalayan range, the northern parts of the Tibet/Pamir Plateaus, as well as the Tien Shan, Altay and smaller Mongolian ranges farther north (Figures 1–3). Overall, the inception of mountain building, sustained topographic uplift and Tertiary magmatism appears to have been generally older in the south than in the north (Figure 2), ranging from early Eocene (Illerdian) in south-central Tibet and Yunnan to Oligocene and Miocene farther north, with the youngest, Plio-Quaternary ranges in Mongolia (e.g., Lacassin et al., 1996; Liu-Zeng et al., 2008; Long et al., 2015; Métivier et al., 1998, 1999; Meyer et al., 1998; Roger et al., 2000; Tapponnier et al., 2001; Vassallo et al., 2007).

Validation: Liqing Jiao, Frédéric-Victor Donzé
Writing – original draft: Liqing Jiao, Paul Tapponnier
Writing – review & editing: Liqing Jiao, Paul Tapponnier

Such northwards younging of relief, deformation and magmatism implies that crustal thickening propagated farther into the Asian continent with India's unabated, ≈NNE-directed indentation. Likewise, the large, principally left-lateral, strike-slip faults, and the Tertiary oceanic-basins/rifts that formed at the ends of these faults (Figure 2) appear to have developed earlier in the south than in the north. The sequential nucleation and growth of the largest strike-slip faults (Red-River, Altyn Tagh) has thus been interpreted to have directed the successive extrusion of the Sunda block, then of Tibet and South China, toward the Southeast and East, respectively (Figure 2) (e.g., Briais et al., 1993; Lacassin et al., 1997; Leloup et al., 1995, 2001; Meyer et al., 1998; Peltzer & Tapponnier, 1988; Replumaz & Tapponnier, 2003; Tapponnier et al., 1981, 1986, 1990). At the southern and eastern ends of the main faults, the opening of large oceanic basins or rifts (South China and Andaman Seas; North-China Plain-Bohai gulf; Wei He-Fen Wei-Shanxi graben; Yinchuan and Baotou graben; Baykal and Hovsgol rifts) contributed to absorb much of the strike slip displacements, with ages, overall extension amounts and rates decreasing from south to north (e.g., Briais et al., 1993; Lacassin et al., 1997; Peltzer & Tapponnier, 1988; Tapponnier et al., 1982). Last by not least, regional inversion of Tertiary deformation, best documented for strike-slip faults (Lacassin et al., 1997, 1998), occurred across large parts of Sundaland and adjacent regions as they were bypassed by India, at a scale unmatched elsewhere across Eurasia. Specifically, such prominent inversion affected the Red River-Ailao Shan shear zone and many thrusts and strike slip faults across Yunnan and the Shan Plateau, as well as normal faults in the rift basins of the gulfs of Thailand and Tonkin (e.g., Darman, 2017; Huchon et al., 1994; Lacassin et al., 1997, 1998; Lai et al., 2012; Le Dain et al., 1984; Mansor et al., 2014; Tapponnier et al., 1986; Wu & Wang, 1988).

Various techniques, generally involving a rigid Indian prong impacting a larger, weaker continent, have been used to model the broad-scale, Tertiary deformation of eastern Asia.

Initial, analog modeling attempts to produce complementary, partly contrasting results. Following insights based on slip-line field theory (Tapponnier & Molnar, 1976), which implied that much of the deformation/faulting resulted from the northward penetration of India into Asia, the first such models (Peltzer & Tapponnier, 1988; Peltzer et al., 1982; Tapponnier et al., 1982) examined the growth of faults due to indentation of a rigid die into a strain-softening material (plasticine) in 2D. While they succeeded in accounting for the generation of large strike-slip faults and cracks (rifts) in eastern Asia (Figures 2 and 3), however, such 2D models could not, by design, address the other main facet of collisional deformation, namely mountain building and crustal thickening. Second generation, 3D analog models (e.g., Cobbold & Davy, 1988; Davy & Cobbold, 1988; Fournier et al., 2004), that included approximate scaling for gravity, met with some degree of success in simulating the growth of mountain ranges across Tibet. However, they generated only one significant strike-slip fault on the NE side of the indenter (e.g., Davy & Cobbold, 1988, Figures 3 and 4), or exceedingly broad swarms of small, conjugate sinistral and dextral faults with minimal offsets (Fournier et al., 2004, Figures 4–7), in strong contrast with those observed in Asia. Further 3D, more sophisticated, two-layered analog models performed at 80g in a centrifuge for dynamical gravity scaling, produced realistic combinations of thrusts and strike-slip faults, but deformation was partly symmetrized by a central shift of the floating block-model due to superficial gravitational warping (Figure 9b in Peltzer, 1988).

Numerical modeling was also promptly introduced to replicate large-scale Asian collisional deformation. Early Finite Element Models with fixed outer boundaries produced wide lithospheric thickening and uplift across smoothly rising and growing highs, with wide, shallow-dipping topographic borders, deemed comparable to the Tibet Plateau (e.g., England & Houseman, 1986; England & Molnar, 1997; Houseman & England, 1986). Save for broadly distributed dextral shear around the eastern corner of the indenter, however, such models produced little deformation akin to strike-slip faulting. Specifically absent were features remotely comparable to the dominant, Eocene to Holocene, left-lateral faults observed within and across the east side of the Tibet plateau (Figures 1–3). Other first-generation FE models simultaneously explored the combined influences of buoyancy forces, a free east-Asian boundary, and a stiff pre-collision inclusion within the Asian continent (e.g., Vilotte et al., 1982, 1984, and 1986). While duly showing that the last two conditions promoted localized, east-directed shear, however, such models also failed to generate the most outstanding faults observed across the collision zone.

Second generation FE models (e.g., Cook & Royden, 2008), also with rigid outer boundaries, included both strong, fixed blocks mimiking stable cratons (e.g., Tarim, South-China) and weak (more seismic) regions (e.g., Yunnan, southern Sichuan), with a stationary indentation front located in the middle of central-Tibet. Not-surprisingly, this produced high topography north and south of that mid-Tibetan front, as well as horizontal shear along the

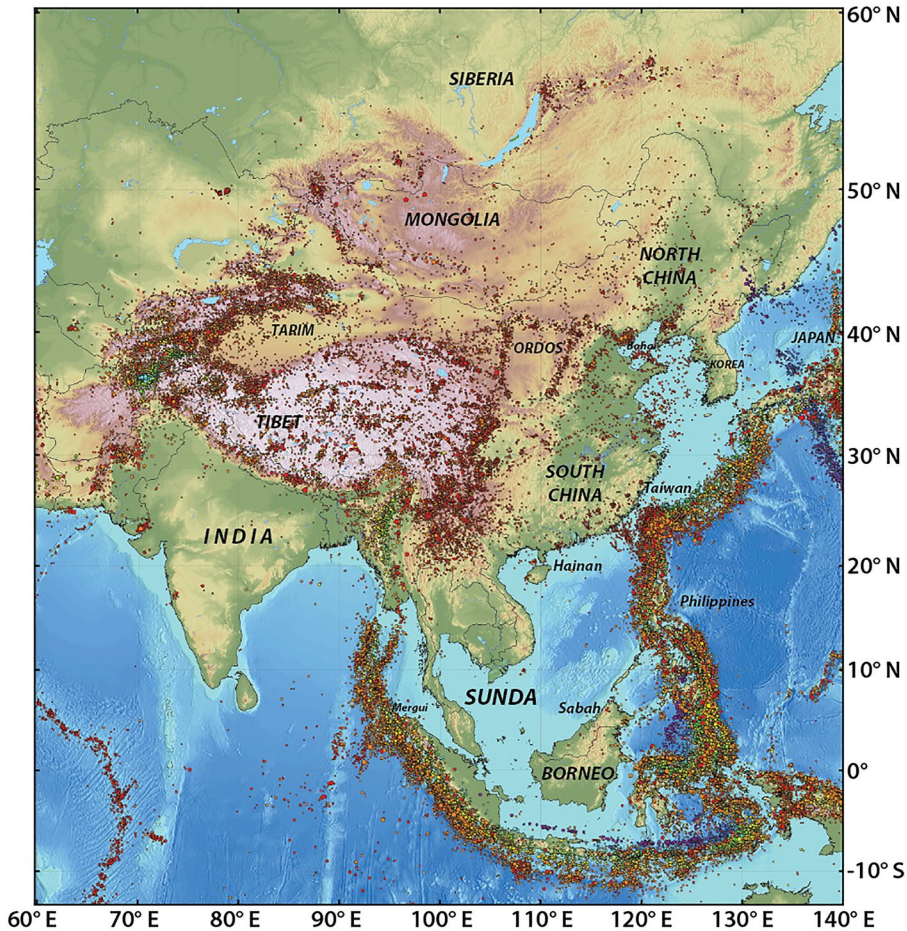

Figure 1. Present-day Southeast Asian topography/bathymetry (color shaded), and seismicity ($M \geq 4.5$, red to violet with increasing depth; courtesy of Yu Wang, EOS, Singapore, 2017). Main regions and country names (black) are indicated.

fixed block boundaries. However, while rightfully exploring, as already attempted by Villotte et al. (1986), the effects of strong rheological contrasts inside the Asian collage (e.g., Proterozoic Tarim and South-China, Mesozoic Indosinian terraines; see also Molnar & Tapponnier, 1981 and Replumaz & Tapponnier, 2003), such models equally failed to engender the prominant strike-slip faults observed within Tibet, or east and south of it. Moreover, neither the Tarim nor South China remained fixed during the collision. GPS data, for instance, now confirm that, relative to stable Siberia, they are presently moving in nearly orthogonal ≈NS and ≈ESE directions at rates of ≈14 and ≈8 mm/yr, respectively (e.g., Wang & Shen, 2019). Additionally, paleomagnetic declination changes imply that large parts of South China have rotated clockwise by ≈12° or more (S. Li et al., 2017), and there is no evidence for a Tertiary, mid-Tibetan, India-Asia suture.

Lastly, whether numerical or experimental, the most recent, sophisticated India/Asia collision models still fail to reproduce the Tertiary faulting observed in and around Tibet, even though they generally consider un-obstructed boundaries around the Asian continent. For instance, active subduction rollback along Asia's Pacific and Sunda rims has been taken into account in analog simulations (e.g., Schellart et al., 2019), and actual subduction along both has been included in recent 3D, FE/DE models (e.g., Capitanio & Replumaz, 2013; Chen et al., 2017; Sternai et al., 2014, 2016). In general, however, such refined models do not generate faults or shear zones with large displacements (≥50 km) inside the continent, away from initially introduced boundaries. Besides, they often produce deformations in blatent contradiction with extant evidence. For instance, Schellart et al.'s simulations (2019) generate strike-slip faulting mostly in areas where little or none exist, or with offsets opposite to those observed. Sternai et al.'s models (2016) cause ≈NS extension in areas of northeastern Tibet (Qilian Shan) where only ≈NE shortening has prevailed since the Miocene (e.g., Meyer et al., 1998; Zuza et al., 2018; Z. Li et al., 2021, 2022).

Figure 2. Schematic large-scale model of Cenozoic faulting and block motions across Southeast Asia (adapted from Tapponnier et al., 1982 and Peltzer & Tapponnier, 1988). Pink, orange and yellow shades outline continental India, Sunda, and China-Tibet. Large open arrows show their approximate Oligo-Miocene and recent motion directions relative to northern Asia. Slimmer colored arrows indicate successive extrusion phases from south to north. Smallest, black arrows are predominant extension directions. Red lines are major active faults, with triangular and straight teeths for mega-thrusts and large normal faults, respectively. Dashed dark-blue lines (with numbers indicating maximum lengths) outline largest strike-slip and extensional block boundaries. Increasing background shades of blue or green mark basins floored by oceanic or thinned crusts around Southeast Asian continental corner.

In summary, the most critical problem with most long-term Asian collision models is that they generally fail to generate the prominent horizontal discontinuities that characterize the deformation of the continent since collision began ≈55 Ma ago, namely the dozen of large strike-slip faults/shear zones (Figures 1–3) that have profoundly shaped its geological and topographic fabric (e.g., Tapponnier et al., 2001).

It is particularly frustrating that none of the 3D models discussed above produces a large left-lateral fault similar to the Ailao Shan-Red River (ASRR)- Yinggehai-Song Hong–QuiNhon-Triton shear zone (Figure 2) (e.g., Leloup et al., 1995). Not only is the ASRR arguably Earth's greatest strike-slip fault zone, both in terms of total

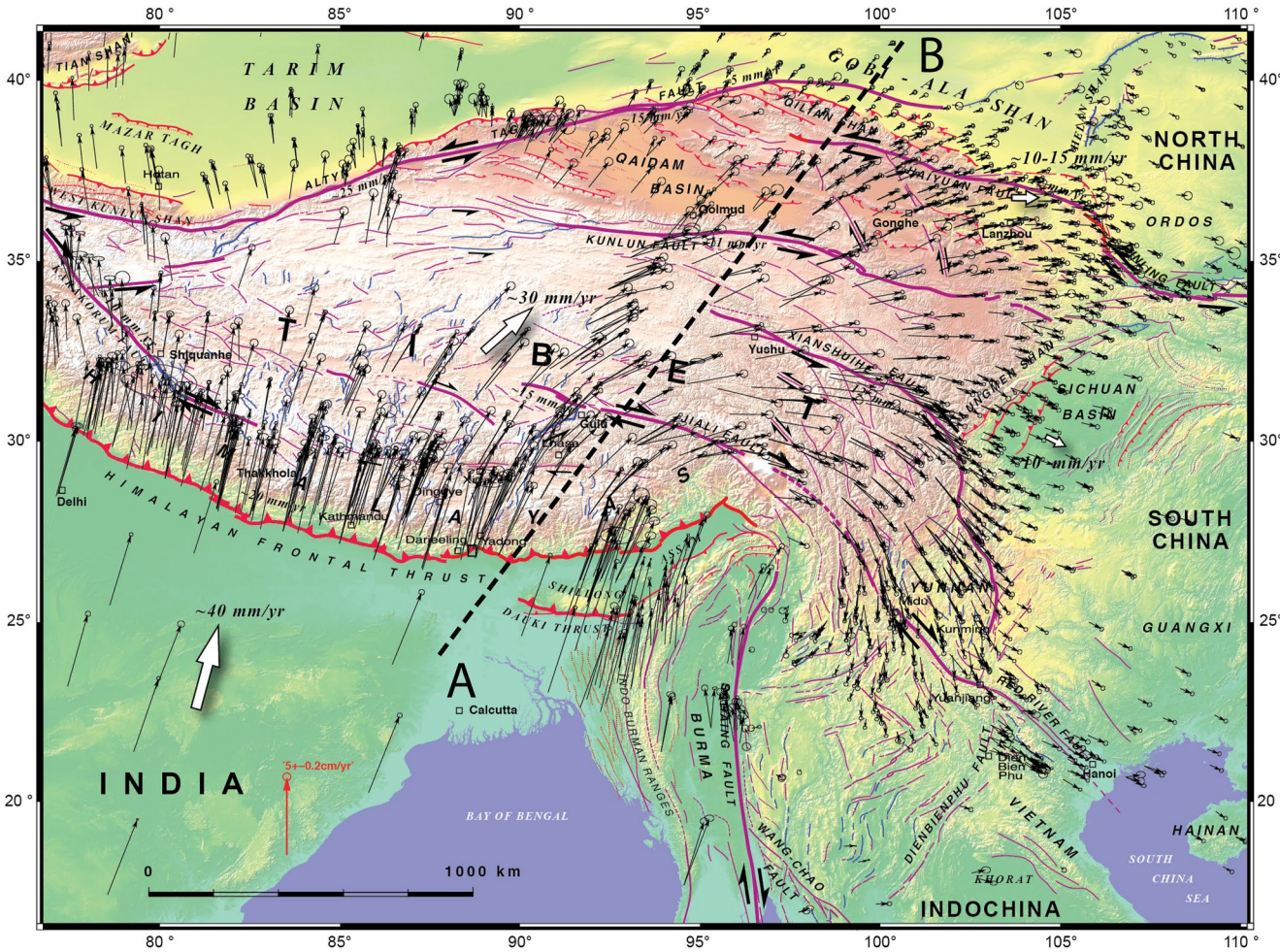

Figure 3. Map of active faults (red, violet and blue for thrust, strike-slip and normal faults, respectively) across Tibet and adjacent regions (updated from Tapponnier et al., 2001). GPS velocity vectors (small black local, and white regional arrows) relative to fixed Siberia are from Kreemer et al., 2014. Topographic shading is similar to that in Figure 1. Thick, dashed black line AB is location of section in Figure 6a.

offset (≈700 ± 100 km) and length (≈4,000 km, from SE Tibet to the southern tip of the coeval, mid-South China sea ridge), (e.g., Briais et al., 1993) but, together with the high Himalayan Main Central Thrust (MCT), it is also the second most prominent high grade, Tertiary (35-15 Ma) metamorphic belt in continental Asia (e.g., Gilley et al., 2003; Leloup et al., 1995, 2001; J. Li et al., 2022; Schärer et al., 1990, 1994; Tapponnier et al., 1986, 1990).

A left lateral shear zone of such outstanding size, at this location, was generated only by the earliest 2D analog plasticine models (e.g., Peltzer & Tapponnier, 1988; Peltzer et al., 1982; Tapponnier et al., 1982), and never reproduced again by any of the more advanced 3D models. That initial 2D approach, strongly ostracized by some, had the obvious limitation of not addressing mountain or plateau building. Conversely however, models designed to simulate crustal/lithospheric thickening and the growth of high relief across the Himalayas and Tibet should not fail to produce the largest Tertiary, left-lateral faults observed across, east and north of the plateau. Clearly, a vital first-order test of success for mechanical models seeking to elucidate large scale Asian tectonics during the last 55 Ma must be that they account for large amounts of BOTH crustal thickening and strike-slip shear where they are irrefutably observed. Thus far, none of the extant models do.

We thus try here to use Discrete Element Modeling (DEM) (e.g., Cundall & Strack, 1979), to explore whether that numerical approach (e.g., Jiao et al., 2018, 2021, 2022) can successfully generate the actual, observed, 3D Asian deformation, including great faults of all types, time-dependent step-by-step topographic uplift in different regions, and the large oceanic basins and rifts that formed around the southeastern corner of the continent since collision began (Jiao, 2016). The model results are then compared to observed fault geometries, ages, slip

amounts and rates, regional seismicity and block motions, and to time dependent topographic uplift, mountain building and related crustal thickening, as well as paleomagnetic inclination and declination changes.

2. 3D Discrete Element Modeling of Asia's Deformation in the Last 55 Million Years

2.1. Methodology and Model Setup

We adapted the Yade DEM code (Šmilauer, 2021) to simulate large-scale, 3D plate deformation, with scaling for gravity and buoyancy (Supplementary Notes 1 to 3, and Figures S1 and S2 in Supporting Information S1). As customary in most models, India is kept rigid while it indents Asia. Since the focus of the model is to explore Asian deformation, we make no attempt at this stage to account for subduction of the Indian mantle beneath the Himalayas and for shortening of the Indian crust (up to ≈15 mm/yr at present) across that range during the last 27 Myrs (half of the total, 55 Ma collision span).

Our 3D DE model is 22.5 m wide, 30 m long and 0.25 m thick (Figure S1 in Supporting Information S1). The deforming Asian plate is modeled as an assembly of 300,000 randomly distributed spherical elements (Figure S2 in Supporting Information S1) with different radius (minimum 29.4 mm, maximum, 54.6 mm; ratio = 1.86 ≈ 2) to avoid crystal lattice effects (Donzé et al., 1994; Plassiard, 2009; Scholtès & Donzé, 2013).

A length of 1 m and a time interval of 1 s in the model represent 500 km and ≈0.124 million years in nature, respectively. The 5 m width of the model indenter is thus equivalent to the ≈2,500 km length of the Himalayan range, and its thickness (0.25 m), to that of the average Asian continental lithosphere (125 km). We take the age of the initial continent/continent collision to be ≈54 Ma, as now widely accepted, and apply a simplified, constant, model indentation rate of 0.01 m/s, scaled to represent ≈4 cm/yr (40.3 km/Myr on average) in nature. Given Asia's large extent westwards and northwards, the western and northern sides of the model are set to rigidly constrain displacements. On the other hand, since they are bounded by long-active subduction zones, the eastern and southern boundaries of the continent are kept free. The actual values of the different parameters used in the 3D DE model are listed in Table S1 in Supporting Information S1.

In the following description of the modeling results, we divide the whole indentation process into 11 stages (6 shown in Figure 4, and all 11 in Figure 5). Such stages are chosen to best illustrate the step by step evolution of distinct features, including large thrusts, strike-slip faults, and rifts. We describe below in greater detail the 6 time-dependent stages shown for each of the 7 different deformation markers (Figure 4) that may be compared, in map view or section, with available ^{4}G observations across Asia. Complete animations of the 3D evolution of the entire model as a function of time are shown in planar overview, transparency, high-resolution, and section in Supplementary Animations 1–4 in Supporting Information S1.

More specifically, Figures 4a–4g successively show overall surface deformation as outlined by passive colored markers (a), lithospheric thickness changes in map view (b) and section (c), element bonds breaking as proxies for seismicity (d), finite displacement vectors (e) (the latest of which potential proxies for ongoing GPS displacements), changes in element-domain's “latitudes” (f), as proxies for paleo-magnetic inclination changes, and angular rotations about vertical axes (g), as proxies for paleo-magnetic declination changes. Figures 5a–5k display in even greater detail the successive initiation, growth and slip-rates of the different types of faults observed in the 11 stages of the model. The complete 3D evolution of deformation and faulting, as deduced from the combined, detailed observation and analysis of the DE model changes in Figures 4 and 5, and Supplementary Animations 1–4 in Supporting Information S1, is described below.

2.2. Detailed Analysis of DEM Deformation, Faulting and Kinematics

Between 54 and 52 Ma in model time-scale (ms) (Figure 4, first column, and Figure 5a), with only ≈80 km of north-south indentation (ms), the Asian plate starts to deform very close to the Indian indenter (Figures 4a and 4b), with a combination of incipient, asymmetric, frontal thrusting and tangential strike-slip faulting (Figures 4c, 4d, and 5a). Thrusting (T1) bounds the growth of an ≈EW trending mountain range that develops just north of the indenter's western front. Incipient right-lateral, NW striking strike-slip faulting (D1) also nucleates north of the indenter's eastern corner. At that stage ≈75% of the shortening has been absorbed by thrusting and the average dextral slip-rate on D1 has been ≈14.1 mm/yr. Note, however, that during that time, broadly distributed movement (and partly elastic deformation?) is also observed to extend as far as 5,000 km north of the indenter front, particularly toward the east (Figure 4e, left).

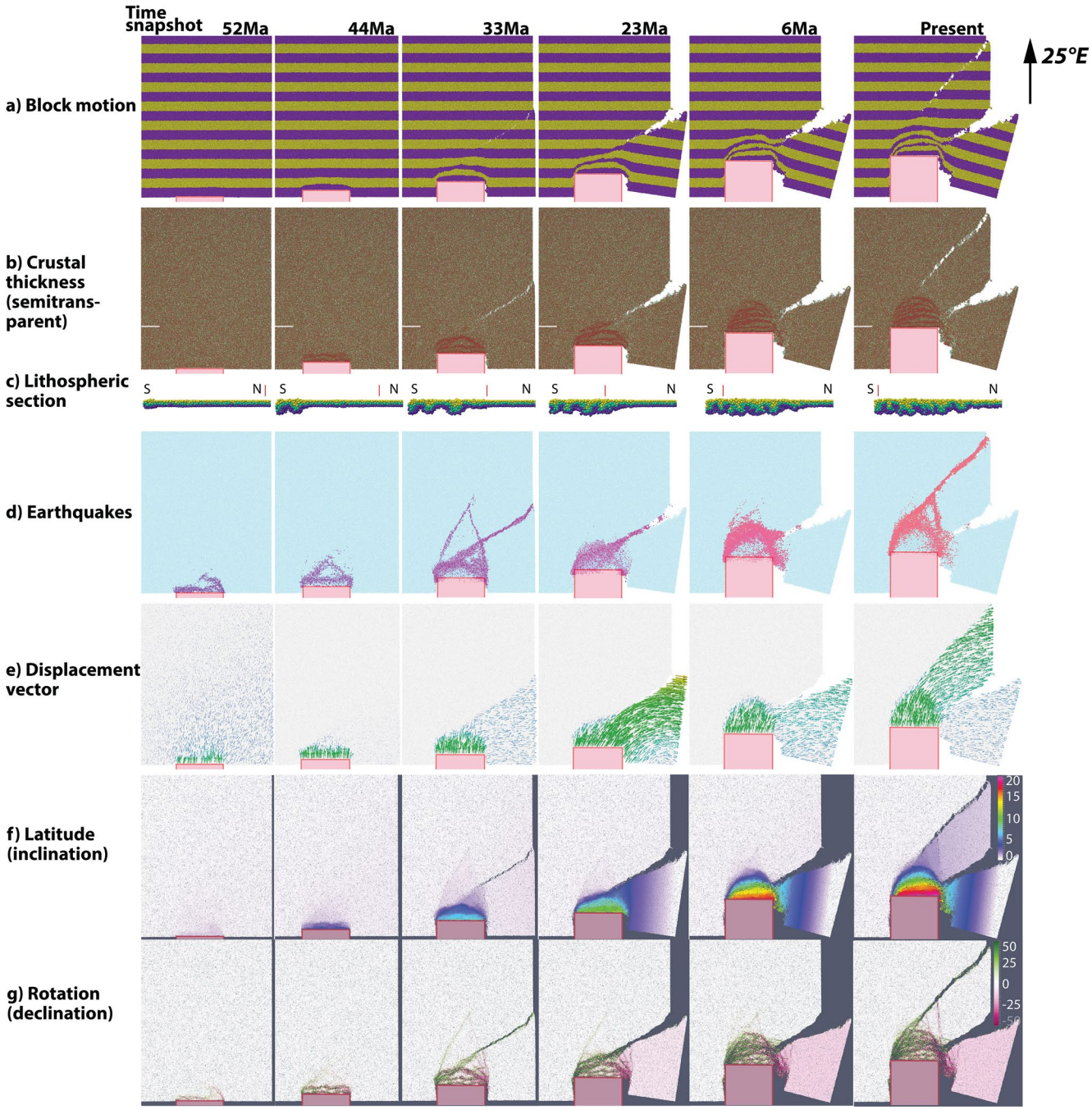

Figure 4. Discrete Element Modeling deformation of model Asia at 52, 44, 33, 23, 6, and 0 Ma stages (model time-scale: "ms"): (a) horizontal shortening and relative motions of extruded blocks, outlined by passive, linear (N115°E-striking), purple and yellow marker-bands, scaled to be 500 km-wide; (b) crustal thickening and thinning (semi-transparent dark-red and blue colors, respectively). Short white lines to the left mark steady position of fixed, red vertical marker in (c); (c) N25°E sections, located in front of indenter axis, displaying stepping, lithospheric thrusting; Indenter moves from left to right; Vertical red marker indicates position of fixed white model marker in (b); (d) "Micro"-crack distribution (≈"ms" earthquake proxies); Purple to red colors outline successive crack activation from 54 Ma to present; (e) Finite surface displacement vectors (ms GPS proxies) during successive "ms" periods (54–52 Ma ago, 46 to 44 Ma, 40 to 33 Ma, 31 to 23 Ma, 14 to 6 Ma, and 6 Ma to present. (f) Successive changes in "ms" paleo-latitudes (≈ magnetic inclinations) in degrees, and (g) Successive finite "ms" rotations (≈ magnetic declinations) in degrees.

By 44 Ma (ms), after ≈400 km of convergence (ms) (Figure 4, second column, and Figures 5b–5d), the initial mountain belt has broadened northwards and propagated along the entire indenter front, accommodating NS shortening on two distinct, front parallel (EW), south-dipping thrusts (T1 and T2) that extend to the base of the model lithosphere (Figures 4b–4d, and 5g; Supplementary Animations 1–4 in Supporting Information S1). The

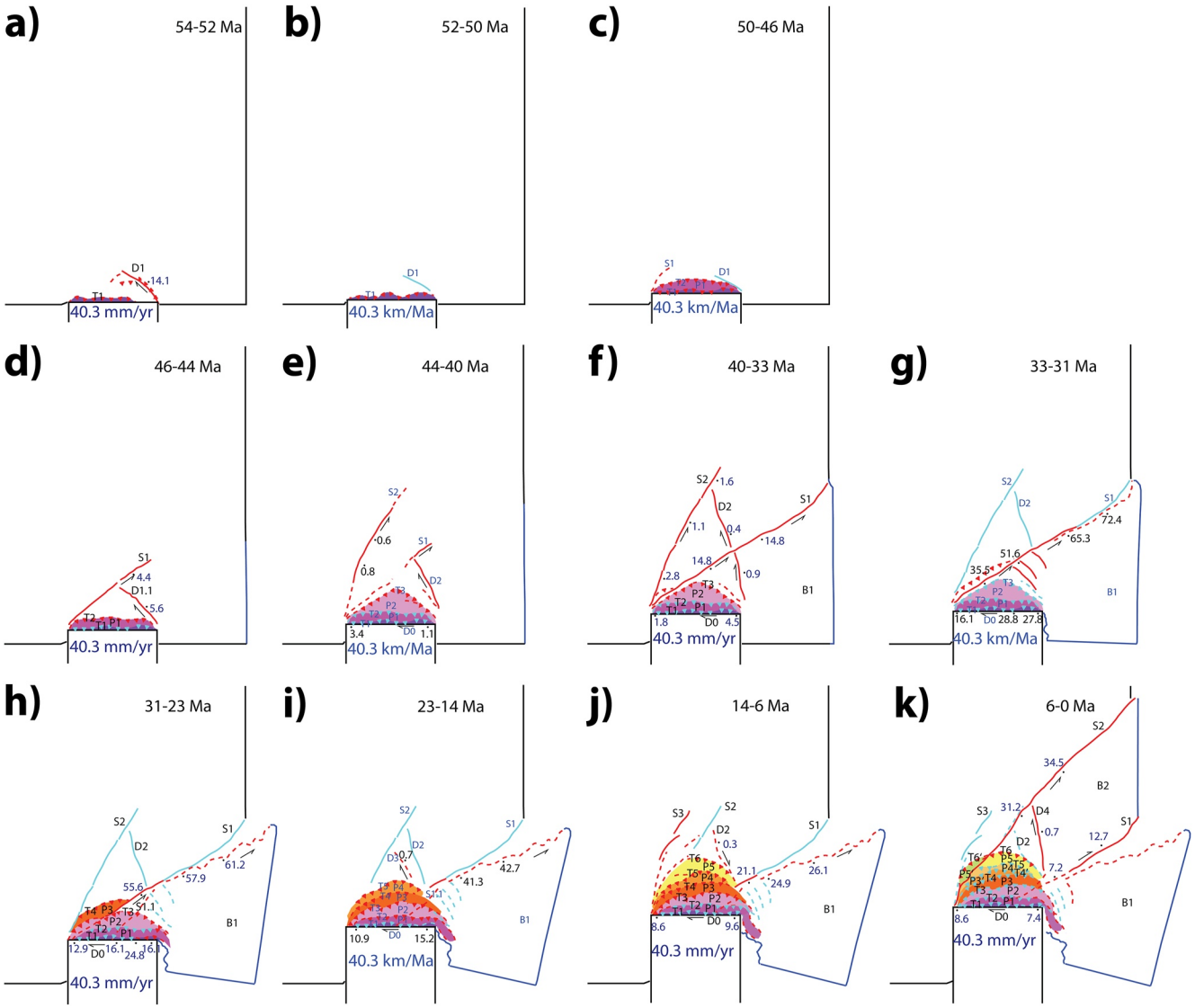

Figure 5. Progressive, northwards ("ms") development of thrusts, strike-slip faults and open cracks during 11 successive stages of increasing indentation. Colored polygons (violet to yellow from older to younger) outline successive isolation of "ms" sub-plateaus (P1 to P5) between rising "ms" mountain ranges and thrusts (T1 to T6'). Red/blue lines and dashed teeth are active/inactive strike-slip faults (S: sinistral; D: dextral) and thrusts (T), respectively. Small numbers indicate "ms" slip-rates (in mm/yr). B1 and B2 are large, successively isolated, model blocks.

two corresponding thrust ranges isolate a narrow basin (P1). Two conjugate strike slip faults are now observed north of the thrusts. In addition to D1, whose average slip-rate has decreased to ≈5.6 mm/yr, a first left-lateral, NE-striking, strike-slip fault (S1) has propagated from the indenter's northwest corner to already slightly bypass the northwestern tip of D1. The average sinistral slip-rate on that fault is ≈4.4 mm/yr. Finally, incipient thrust faulting appears to be nucleating near the southwestern tip of S1 and a small component of thrusting (future T3) partly absorbs displacement near D1's northwestern apex (Supplementary Animations 2–3 in Supporting Information S1). Note also that the far north-reaching, broadly distributed deformation has mostly disappeared at this stage (Figure 4e).

Between 44 and 33 Ma (ms), with up to ≈840 km (ms) of indentation by the model's Indian prong, the left-lateral strike slip fault S1 is observed to propagate all the way to the model's eastern boundary (edge of the model's Asian plate, Figure 4 third column and Figures 5e and 5f). At 33 Ma, with an average rate of ≈15 mm/yr and with a cumulative offset of ≈120 km since 40 Ma, S1 contributed to absorb ≈85 km of convergence, a significant fraction (≈20%) of the total indentation shortening (440 km) during the corresponding 11 million years. For the

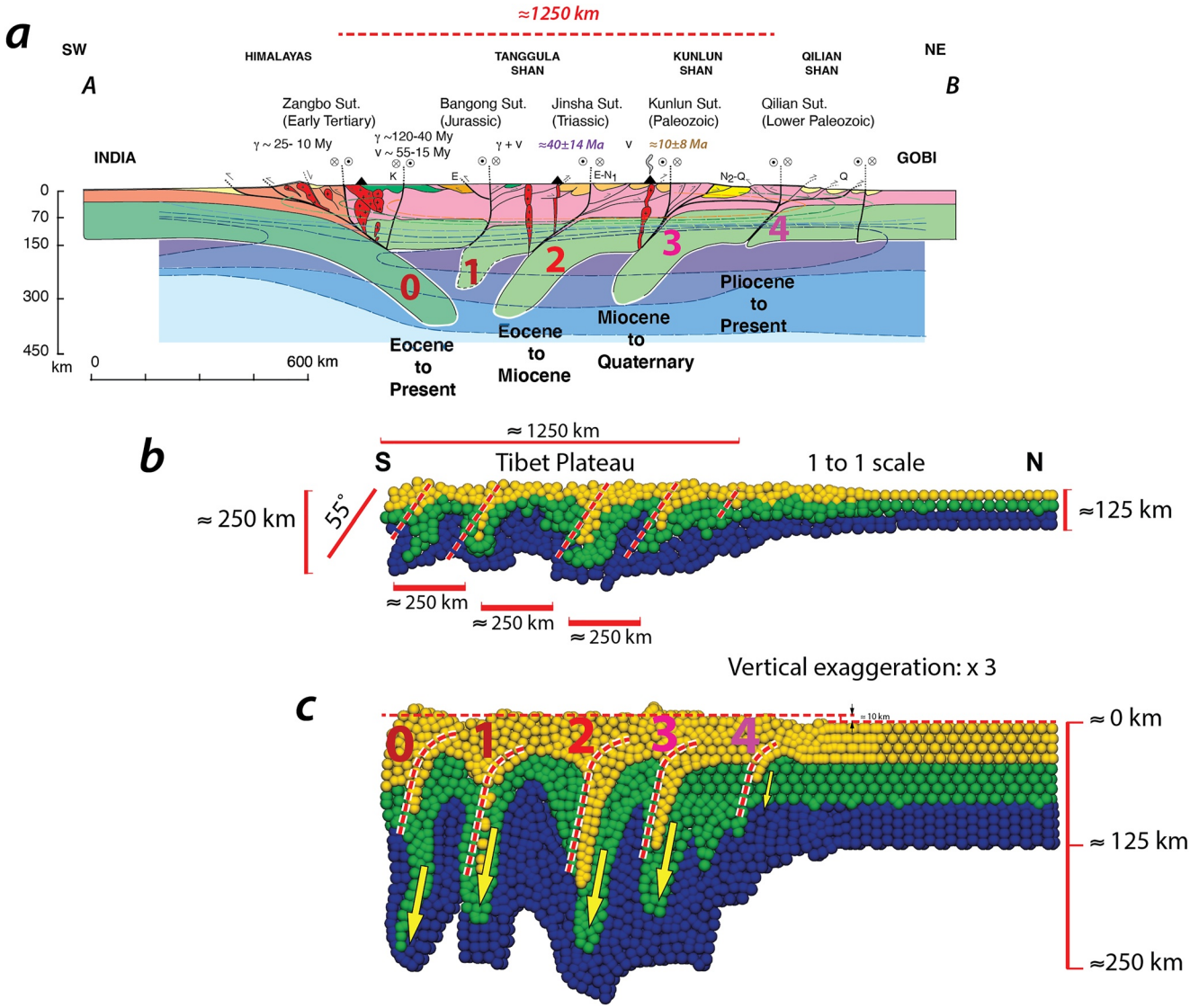

Figure 6. Comparison between section across widest, central-eastern part of Tibet plateau (A-B, Figures 3 and 8), and model results. (a) Simplified lithospheric, geological section across ≈1,250 km-wide central/eastern Tibet plateau, between Zangbo and Qilian sutures. Pink and dark-blue shaded area's lower limits follow seismological bases of crust and lithosphere, respectively (after Tapponnier et al., 2001). 3G data across plateau are consistent with successive reactivation, from south to north, of 4 Phanerozoic sutures, leading to Asian mantle subductions (numbered 1 to 4) during the Tertiary, with associated, north-younging magmatism (from 120 My to present). (b, c) DE modeling produces 4–5 south-dipping subduction zones, ≈250 km apart, reaching maximum model depths on order of ≈250 km. In section c, the vertical scale is exaggerated by x3, and the number of model elements is increased for clarity.

first time, en-echelon "cracks" are observed to open, and broaden northwards, along the north-eastern half of S1, all the way out to the model's eastern boundary (Figure 4b). Such cracks, that start forming late (≤≈35 Ma, ms) reflect wholesale (≈lithospheric) block rifting due to NW-SE directed extension near that boundary. The region east of the indenter is now entirely surrounded by faulted boundaries, hence isolated as a coherent block (B1, Figure 5f). That block has started to move eastwards, ≈orthogonally to the mostly northwards displacement of the region just north of the indenter (Figure 4e). Incipient eastward motion is also observed along the indenter's front (D0), as attested by increasing dextral slip from west to east (1.8–4.5 mm/yr, Figure 5f) along that front.

Even though, at this stage, as predicted by slip-line field theory (Backhofen, 1973; Johnson et al., 1970), two conjugate, almost symmetrical strike-slip faults (S2 and D2), with small total offsets (≈5–20 km) and slow rates (1.1–2.8, and 0.4–0.9 mm/yr, respectively), have nucleated and propagated more than ≈3,000 km northwards, the dominant faulting and deformation have become strongly asymmetric (Figure 4, third column and Figure 5f, and Supplementary Animation 3 in Supporting Information S1).

As in previous stages, the largest fraction of the indentation shortening (now ≈355 km, ≈80%) has been absorbed by crustal thickening. A new, large, south-dipping thrust (T3), extending to the base of the model's lithosphere (Figures 4b, 4c, 4g, and 5f), has taken up much of that shortening, while additional, more local thrusting is also observed north of the indenter's two corners (Figures 4b, 4d, 4g, 5f, and Supplementary Animations 2–3 in Supporting Information S1). A new, sizable sub-plateau (P2) is now isolated between mountain ranges T2, to the south, and T3, to the north (Figures 4b, 4c, 4g, and 5f), (Supplementary Animation 3 in Supporting Information S1).

During the next 10 million years, ***between 33 and 23 Ma*** (ms), with ≈400 km of additional northward motion of the model's indenter, the deformation of the model's Asian plate is dominated by the eastward extrusion of block B1. Except near its western tip, B1 remains fairly stable, internally, as it splits apart from the also mostly stable northeastern half of the model's Asian plate (Figure 4, fourth column and Figures 5g and 5h). Much (especially the eastern part) of the region of previously thickened crust north of the indenter (ms "Tibet") is also pushed obliquely toward the northeast, roughly in tune with the rest of B1 (kinematic motion vectors in Figure 4e). Left lateral movement along fault S1, that now strikes ≈N60°E on average (in the model framework, mf) and extends northeastwards over a length of ≈5,000 km, dominates the deformation field. From west to east, the slip-rate along much of that fault increases from ≈50 to ≈60 mm/yr (Figures 5g and 5h). The large finite displacement along the fault has split apart the eastern boundary of block B1 from the stable edge of the northeastern Asian model plate. This has opened a ≈700 km wide crack (≈"rift") that strikes more northerly (≈N40°E, mf) than S1. Concurrently, block B1 has also rotated by up to ≈8° clockwise (Figures 4e and 4g, fourth column, and Figure 5h). Note that the dominant motion along S1 has impeded further slip on S2 and D2, which have mostly, though temporarily (see below), been "de-activated" (Figure 4d, fourth column, and Figures 5g and 5h). Also, a secondary southeastern branch of S1 (S1.1, Figure 5h) now crosses the mid-eastern part of the thickened crustal region in front of the indenter (Figure 4d, fourth column).

Toward the south, along the front of the indenter, the extrusion of B1 and of the thickened crustal area in its western part has led to dextral faulting (D0), at rates that increase eastwards from ≈13 to 16-24-16 mm/yr (Figures 5g and 5h). Consequently, block B1 has thus also split apart from the eastern edge of the indenter. This has opened another crack (≈"rift"), ≈200–300 km wide (ms), between the southwestern rim of B1 and the eastern edge of the indenter (Figures 5g and 5h). That dextral displacement along D0 has thus moved part of the thickened crust in front of the indenter past its eastern corner, away from the direct impact of colliding model India. There has also been significant deformation inside the sheared western tip of B1, particularly along several short, NNW-striking dextral faults (one of which formerly the southern segment of D2) (Figures 5g and 5h).

Last but not least, northwest of the indenter and north of S1, a fourth, south-dipping thrust fault (T4) has contributed to uplift a new mountain range north of a new inter-mountain sub-plateau basin (P3) (Figures 4b–4d, 4g, and Figure 5h). This youngest topographic high lies distinctly northwest of T1-T3 and P1-P2, all of which bounded northwestwards by S1 (Figures 4g and 5h).

In the following 17 million years, ***from 23 to 6 Ma*** (ms), with up to a total indentation of ≈1,900 km (Figure 4, fifth column, Figures 5i and 5j, and Supplementary Animations 2–3 in Supporting Information S1), the unabated eastward extrusion of block B1 continues. Even though the left-lateral slip-rate along S1 slows down to ≈21–26 mm/yr in the second half of that period, the total "rift" separation between B1 and stable NE Asia now reaches up to ≈1,400 km, and the total clockwise rotation of B1, ≈15 ± 2.5°. Coevally, with continued dextral faulting along the indenter's front (D0), at a rate of up to ≈10 mm/yr, B1 kept moving southeastwards away from the indenter's eastern corner. That separation (up to ≈700 km) was accompanied by the continued opening of a ≈700–800 km long, V-shaped notch penetrating up to ≈400 km into B1's western margin (Figures 4a, 4b, and 4d–4g, fifth column, and Figure 5j). North of that "rifted" crack, within the deformed western tip of B1, faulted smaller sub-blocks rotated clockwise by as much as 40 ± 20° (Figure 4g, fifth column).

That period of indentation is also characterized by the rapid development, north of S1, of three south-dipping thrusts (new T5 and T6, north of growing T4), with the associated rise of high mountains and isolation of intervening "piggy-back" sub-plateaus (P4 and P5) (Figures 4a–4d, and 4g, fifth column, and Figures 5i and 5j). Such northwards relief growth is coeval with the eastwards lengthening of thrusts T2, T3, and T4, the eastwards displacement of S1 and S1.1, and the narrowing of sub-plateaus P2, P3, and P4.

Finally, on the northwest side of the indented region, coevally with the development of thrusts T5 and T6, left-lateral faulting starts propagating NNE-wards along reactivated S2 and new S3 (Figure 4, fifth column and

Figure 5j). Simultaneously, the northern segment of D2 is also mildly reactivated, with a dextral slip-rate of ≈0.3 mm/yr (Figure 5j).

The latest modeling epoch, ***from 6 Ma to the present*** (ms), shows radical changes in faulting and large-scale deformation kinematics (Figure 4, last column and Figure 5k).

The most prominent event is the rapid northeastward growth of the new sinistral fault S2 all the way to the north-eastern boundary of model Asia (Figure 4, sixth column, and Figure 5k). In little more than ≈6 Ma (ms), S2, which resembles S1, propagates over ≈6,000 km, at a rate on order of ≈100 cm/yr, to reach and offset the east Asian model margin by ≈150–200 km. The average left lateral slip-rate along this ≈N45-50°E-striking fault (mf) ranges between 31.2 and 34.5 mm/yr. Together with the 10°W (≈NS) striking, slower (≈0.7 mm/yr), dextral fault D4 (Figures 4d and 4g) and the thrust (T6) farther west, S2 now isolates a second large, east Asian model block (B2). As it moves rapidly eastwards, that block has also started to rotate clockwise, by ≈1–2° (0.75 ± 0.25°) (Figures 4e and 4g). That rotation has been coeval with the opening of cracks ("rifts") along its northeastern stretch (Figure 4), as was the case along S1 between ≈35 and 23 Ma (ms).

The other remarkable event at this stage is the clear reversal, from left- to right-lateral, of strike-slip motion along S1 (Figure 4e, sixth column). Not only has the eastward extrusion of B1, together with further rift-like opening of the separation between B1 and B2 (both originally part of stable NE Asia) stopped, but the entire regional kinematics has been inverted. In only the last ≈6 million years, S1 slips dextrally by ≈60 km at an average, eastward increasing rate on order of 10 ± 3 mm/yr (Figure 5k). Coevally, dextral slip at a rate on order of 8 ± 0.6 mm/yr continues along the front of the indenter (Figure 5k). Simultaneously, on the northwestern-most side of the indented region, the most recent thrust range and associated sub-plateau (T7 and P6) have now fully developed along and north of S2 (Figure 4g, last one, and Figure 5k).

3. Comparison Between the 3D DE-Model Results and ^{4}G Eocene to Present Tectonic Observations Across Southeastern Asia

The 3D Discrete Element Model results described above (Figures 4 and 5) may be both further refined, and compared to first order, post-Cretaceous deformation and tectonic features observed across the East Asian collision zone (Figures 6–9).

Such a comparison must remain general, at best semi-quantitative, since our simplified modeling approach treats the Asian lithosphere as an homogeneous layer with uniform mechanical properties and initial thickness, bordered by orthogonal limits with over-simplified ('free") kinematic boundary conditions.

That simplicity may be regarded as a significant drawback since it has long been recognized that there are substantial differences in the rheological properties of the blocks of different ages welded into the Asian continental collage since the Archean (e.g., Figure 8). As long pointed out, such differences must influence the strength and rheology of the continental lithosphere, and hence regional deformation patterns (e.g., Cook & Royden, 2008; Molnar & Tapponnier, 1981; Peltzer & Tapponnier, 1988; Replumaz & Tapponnier, 2003; Tapponnier et al., 1986).

That the model's properties and boundary conditions are simple, however, and that it is a 3D approach scaled for gravity (Supplementary note 3 in Supporting Information S1), implies that the results should be robust enough to help clarify the overall development of East-Asian faulting and mountain building. One remaining caveat is that, at this stage, and as in several other large-scale modeling attempts, peripheral subduction (of India and other oceanic plates surrounding Sunda and China) as well as proper seafloor spreading (in the South-China and Andaman seas) (Figure 1) are either ignored or crudely mimicked by proxies.

Finally, the fact that the model does not take erosional processes into account is unlikely to be an irredeemable short-coming since the largest part of the Tibet plateau (≈3/4th, west of ≈95°E), appears to have been internally drained since at least the mid-Miocene (e.g., Liu-Zeng et al., 2008) (Figure 7).

In any case, for now, the limited number (300,000) and large average size of the elements (>50 km) precludes comparison with "detailed" (10 Km-scale) structural field observations or geophysical inferences.

3.1. Five Main Mountain Ranges and Thrusts Bounding Five Tibetan Sub-Plateaus

During the DEM's 54Ma-long timespan, the penetration of the model's Indian indenter into the model's Asian plate consecutively generates 5 main mountain ranges (T1-2 to T6), that young northwards away from the

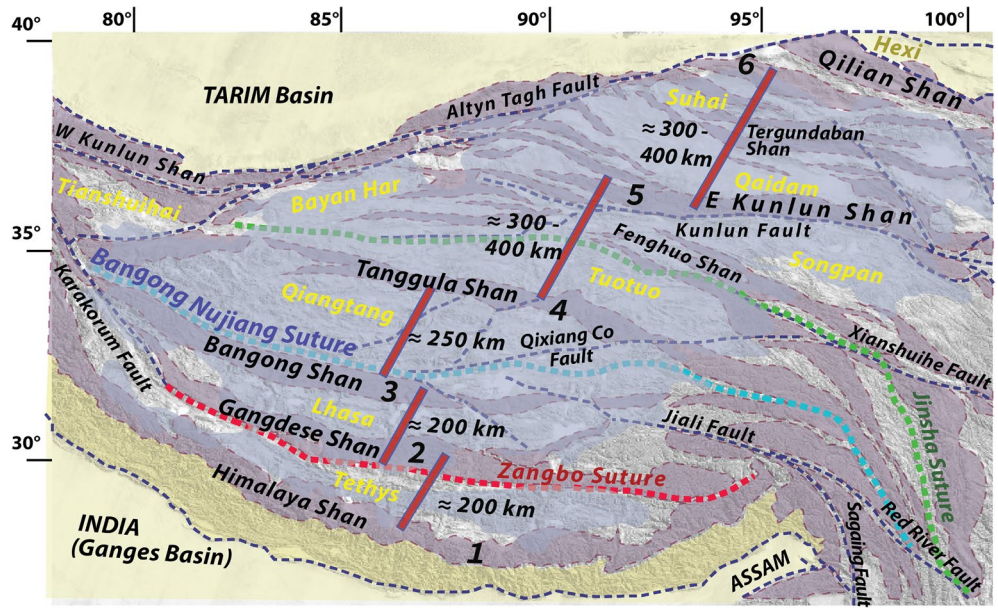

Figure 7. Simplified tectonic topography of central Tibet, superimposed upon digital elevation model of southern collision zone. Yellow-shaded areas correspond to Lesser Himalayan frontal topography. Lighter yellow outlines Tarim Basin, Hexi Corridor, and India's Ganges and Assam foreland basins. Dark pink-shaded bands highlight highest mountain ranges ("Shan", names in black) across central Tibet. Red bars with numbers indicate approximate widths (from ≈200 to ≈400 km) of flatter, high-altitude, basin-like areas (yellow names) between the Tibetan ranges. Largest active faults (named) are dashed dark-blue. Main, trans-plateau suture-zones (Zangbo, Bangong, Jinsha-Kunlun) between Himalayan and Kunlun mountain ranges are also outlined (dashed red, blue, and green colors). Superimposed, light-gray shaded area delineates Plio-Quaternary to present internally drained regions.

indenter's front (i.e., the Yarlung-Zangbo suture, since the model does not address the rise of the Himalayas, that belong to deformed India) (Figures 4–9, and Figures S3–S4 in Supporting Information S1). From left to right in the model, the ranges' spacing varies between ≈200 and ≈300 km (Figure 9, on average ≈250–270 km in Figures 6b and 6c, and Figure S4 in Supporting Information S1), and their average strikes bend mostly by up to ≈50° (Figures 5 and 9, Figures S3 and S4 in Supporting Information S1). Most of them curve strongly clockwise toward the southeast, as do, east of ≈95°E, several of the principal Tibetan ranges (Bangong, Tanggula, Fenghuo, Kunlun, Qilian Shan) (Figures 3, 7, and 8).

The 5 main ranges and megathrusts (T2 to T6) inside the 3D model plateau (Figures 5, 6, and 9) clearly result from under-thrusting of the model's Asian crust/lithosphere, along ≥1,500 km-long, 45–60° south-dipping subduction interfaces that reach maximum depths of 250–300 km (Figures 6b and 6c, and Supplementary Animation 1 and 4 in Supporting Information S1). While the DEM resolution is insufficient to fully assess topographic relief, most of the areas between the mountain ranges in the model are uplifted (see region between thrusts 0 and 4 in Figure 6c section - vertical exaggeration x3-, whose average elevation is ≈10/3 = 3.3 km). The model results are thus consistent with the isolation, between the ranges, of 4–5 high "basins" (sub-plateaus P1 to P5, Figures 8 and 9, and Figures S3 and S4 in Supporting Information S1), that may be interpreted to correspond to the flat-test high "plains" of Tibet (North Lhasa, Qiangtang, Tuotuo, Songpan, and Qaidam-Suhai basins, Figure 7). Such results are in keeping with the geomorphic/tectonic interpretation of plateau growth proposed by Meyer et al., 1998, Métivier et al., 1998, 1999, and Tapponnier et al., 2001).

The deep crustal roots subducted beneath the ranges in the model are fairly regularly spaced (Figures 6b and 6c and Figure S4 in Supporting Information S1). Such separation (≈250–300 km on average in the model, Figure 6 and Figure S4 in Supporting Information S1), as well as the widths of the inter-mountain sub-plateaus in Tibet (200–300 km, Figure 7) may be correlated with, and hence mechanically related to, Tibet's average lithospheric thickness (≈250–300 km, e.g., Griot et al., 1998), as previously pointed out in other modeling studies (e.g., Cobbold & Davy, 1988; Davy & Cobbold, 1988).

Overall, the structure, in section, of the deformed Tibetan lithosphere in the DE model (Figure 6b) is similar to that consistent with geological/geophysical evidence across the central part of Tibet (section AB in Figures 8,

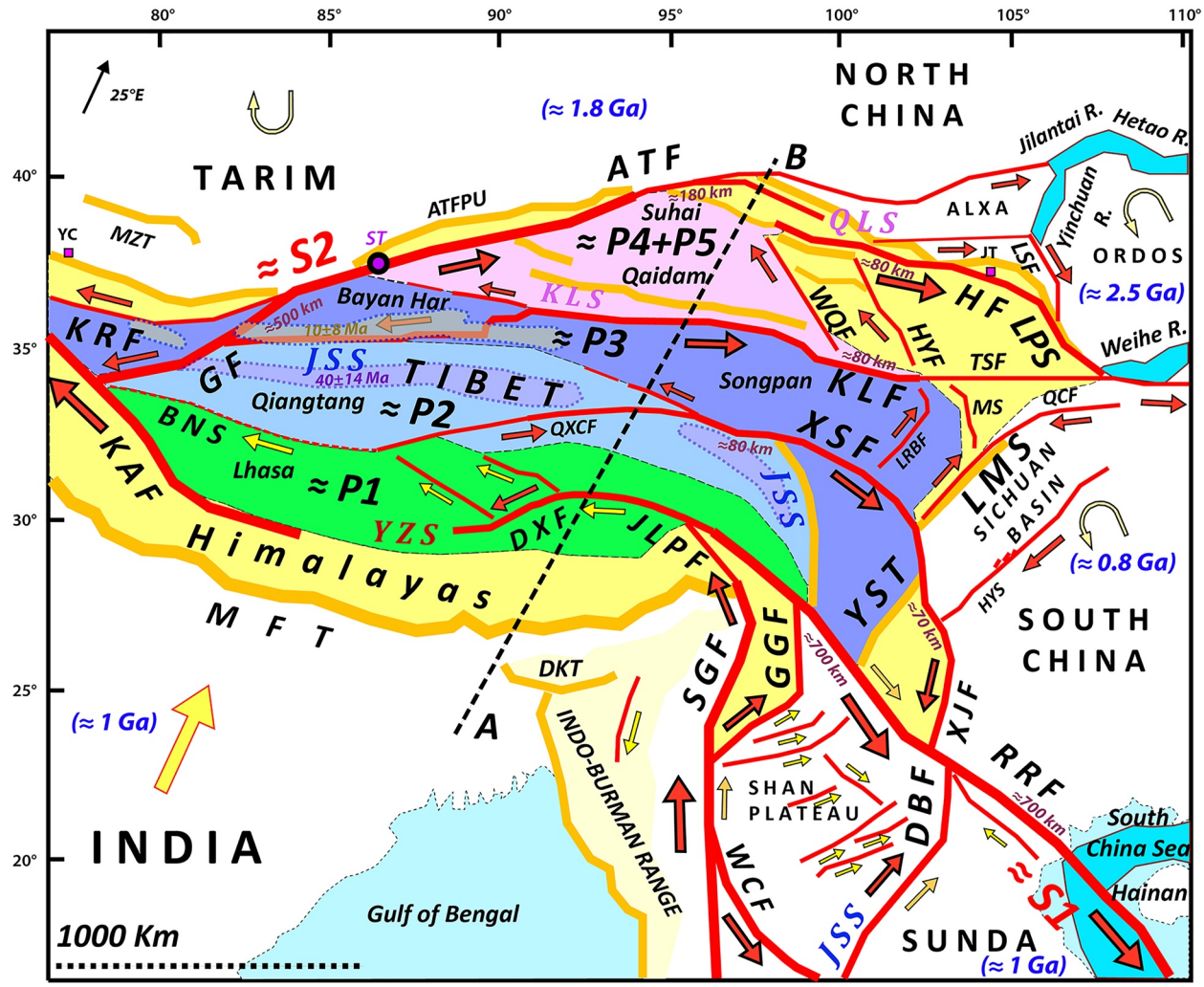

Figure 8. Simplified map of most prominent Tertiary and active faults (red: mostly strike-slip; yellow: mostly or partly thrusts) in Tibet and adjacent regions to the east (mostly after Tapponnier & Molnar, 1977; Peltzer & Tapponnier, 1988; Armijo et al., 1989; Gaudemer et al., 1995; Leloup et al., 1995; Lacassin et al., 1997; Meyer et al., 1998; Vanderwoerd et al., 2002; Lasserre et al., 2002; Tapponnier et al., 2001; Chevalier et al., 2005; Xu et al., 2009; Liu-Zeng et al., 2008; Li K. et al., 2018; H. Li et al., 2021; Z. Li et al., 2021; and references therein). Red arrows along strike-slip faults (larger for faster slipping) indicate sense of predominant Cenozoic movement. Small yellow arrows specify present-day motion where inverted (including on small Shan Plateau faults, Lacassin et al., 1998). Late Cenozoic normal faults with finite offsets ≤20 Km (mostly in Tibet and Yunnan), and north Himalayan STDS (South Tibetan Detachment System), are not represented. Large, partly rising mountain ranges and areas surrounding the Tibet Plateau are shaded yellow. The long Tibetan sub-plateaus (labeled P1 to P4+P5 and colored green, light and dark blue, and pink, from south to north), north of the Tethys-Himalayas and Yarlung-Zangbo suture (YZS), correspond to the Lhasa, Qiangtang, Songpan (also Ganze/Bayan-Har/Tianshuihai), and Qaidam/Suhai terranes, limited/separated by the southwards younging Bangong-Nujiang (BNS), Jinsha (JSS), Kunlun (KLS), and Qilian (QLS) sutures, and by the Tanggula and Fenghuo ranges within central Tibet (Figure 7). The North China (peri-Ordos), and South China Sea rifts are shaded bright blue. The two narrow, elongated, light violet and orange shaded zones south of the JSS and KLS, respectively, delineate the extent of the ≈40 ± 14 and 10 ± 8 Ma-old intrusive and volcanic mid-Tibetan belts. From North to South, the names of the main Tertiary/active strike-slip and thrust faults (with slip-rates ≥3 and 1 mm/yr, respectively) are labeled as: MFT, Main Frontal Thrust; RRF, Red River Fault (≈S1); ATF, Altyn Tagh Fault (≈S2); ATFPU, Altyn Tagh Fault Pushup; HF, Haiyuan Fault; LPS, Liu Pan Shan Thrust; LSF, Luo Shan Fault; WQF, Wenquan (or Elashan) Fault; HYF, Haiyen (or Riyueshan) Fault; KRF, Karakax Fault; MZT, Mazar-Tagh Thrust; GF, Goza Fault; KAF, Karakorum Fault; KLF, Kunlun Fault; TSF, Tianshui Fault; QXCF, Qixiang Co Fault; XSF, Xianshuihe Fault; XJF, Xiao Jiang Fault; HYS, Huaying Shan Shear Zone; MS, Min Shan Fault; QCF, Qingchuan Fault; LMS, Longmen Shan Thrust; LRBF, Longriba Fault; YST, Yulong Shan Thrust; SGF, Sagaing Fault; GGF, Gaoligong Fault; JLPF, Jiali Po-Cu Fault; DXF, Damxung Fault; DBF, Dien Bien Fu Fault; DXT, Dauki Thrust; WCF, Wang Chao or Mae Ping Fault. Small circle dubbed *ST* is Sulamu Tagh. Small squares YC and JT are Yecheng and Jingtai towns. Small red numbers (in km) along some strike-slip faults are most likely finite Tertiary offsets. Precambrian craton's ages (Ga) around Tibet are shown in blue. Yellow circular arrows indicate counterclockwise, and clockwise senses of rotation of Ordos/South China and Tarim blocks, respectively (e.g., Avouac & Tapponnier, 1993; Middleton et al., 2016). Dashed black line A-B is location of section in Figure 6. See related descriptions and discussions in text.

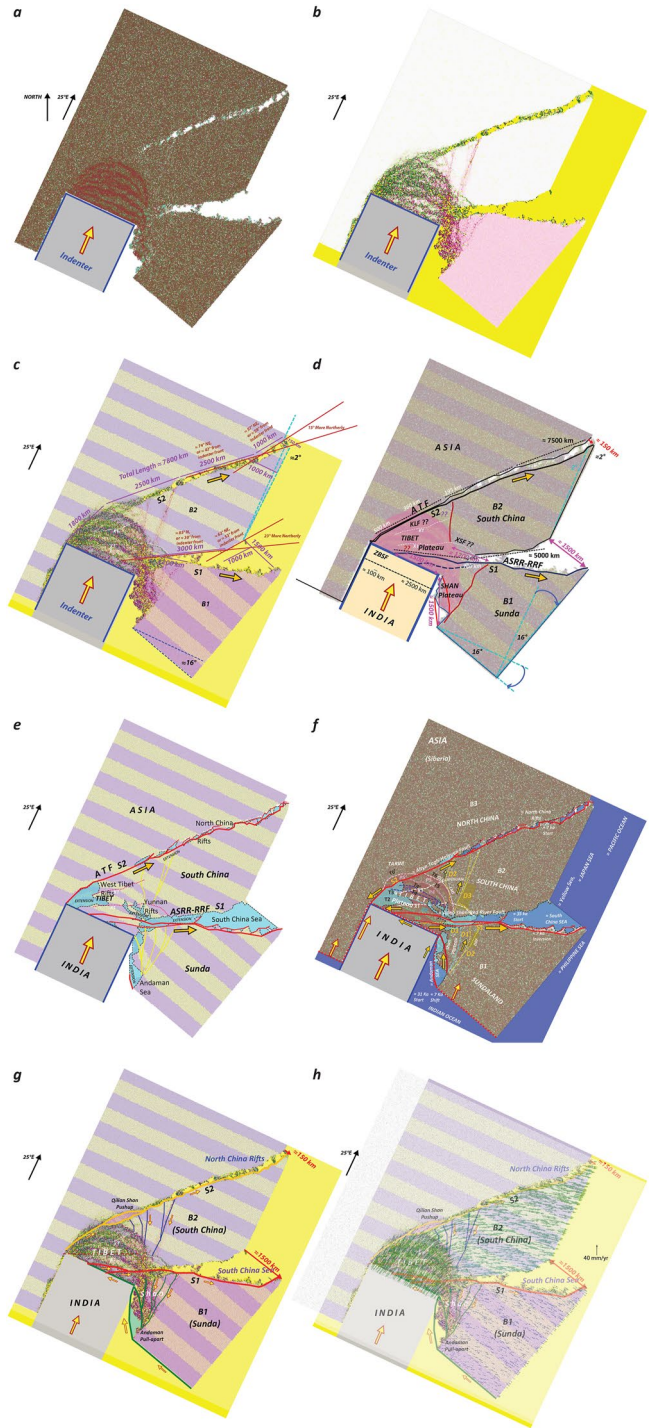

Figure 9.

and 6a, adapted from Tapponnier et al., 2001). Along that section, the actual broad plateau construction also appears to have been divided into that of 4–5 sub-plateaus separated by large mountain ranges (Figures 7 and 8). Added complexity, however, arose from the fact that some of the Tibetan ranges partly follow more ancient sutures and/or are offset by large strike-slip faults (Figure 8), as further discussed below.

At a greater level of detail, in the DE model history of Figures 4 and 5, T1, which forms at the beginning of indentation (≈54 Ma) along the collision front and India/Asia boundary, may be interpreted to reflect shortening along the Zangbo Suture and Gangdese range (e.g., Yin et al., 1994) (Figures 5a, 5b, and 7). In the Linzhu (Lhunzhub)

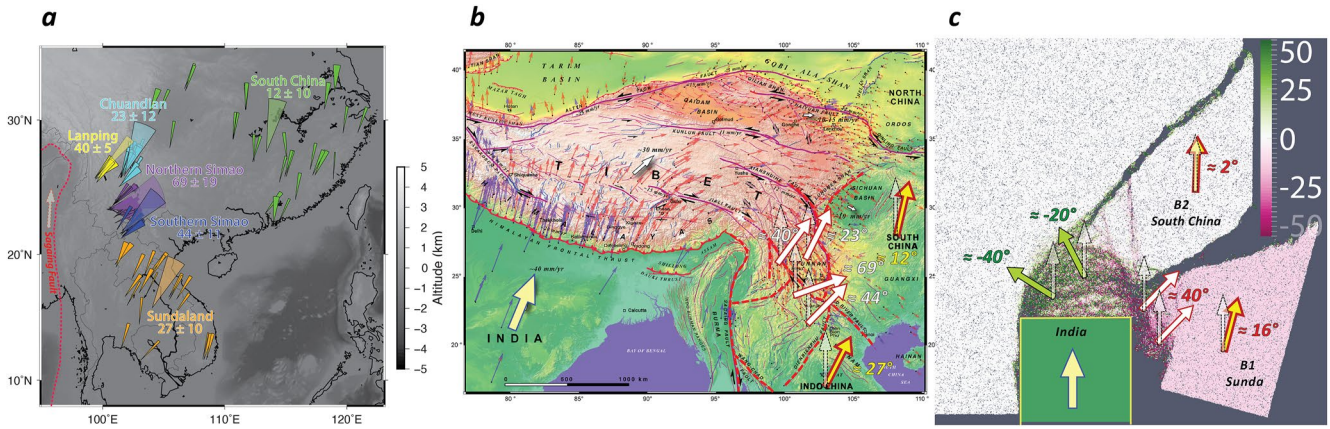

Figure 10. Paleomagnetic declinations (mostly post Jurassic to Late Tertiary red beds) across continental southeast Asia (after Li S. et al., 2017). (a) Regional data (compiled away from major faults) of S. Li et al. (2017) across parts of Thailand, Laos, Vietnam, and South China. Note relatively uniform rotation values, with fairly small uncertainties, across mostly stable South China and Sundaland blocks. (b) Average regional declinations (from data shown in (a)), plotted atop East-Asian Tertiary fault map of Figure 3. (c) Predicted average terrane rotations from DE modeling results shown in Figure 4g, six column.

basin, ≈35 km north of Lhasa, the strong folding of the Cretaceous Takena red-beds and post-depositional warping/thrust-faulting of the Paleocene Lingzizong ignimbrites (e.g., Tapponnier et al., 1981, and references therein) also mark the first major phase of collision-related shortening within the Lhasa block.

T2, which fully starts to develop ≈10 Myr later (≈44 Ma) in the model may be taken to correspond to the folding/thrusting observed along the Bangong-Nujiang suture, at the northern edge of the Lhasa block, and to the correlative uplift (to ≥4,000 m elevation) that was already prevailing in the Lumpo-La basin ≈35 Ma ago (e.g., Rowley & Currie, 2006; Fang et al., 2020). In that same region, a clear, southward dipping tomographic anomaly extending to ≈220–280 km depth beneath the BNS (Tilmann et al., 2003) may be interpreted to reflect subduction of a south-dipping Tibetan lithospheric slab (Meyer et al., 1998; Roger et al., 2000; Tapponnier et al., 2001). That anomaly would thus correspond to Slab 1 in Figure 6.

Model thrust T3 and the associated shortening and thickening that develop clearly around 40 Ma (Figures 4, 5c, and 9; Supplementary Animation 3 in Supporting Information S1) may be compared with the folding/thrusting of Paleogene-Neogene red-beds observed in the central part of the Tibetan Plateau, along the Fenguo Shan, north of the Tanggula arc (Figures 7–9) whose Eocene-Early Oligocene (40 ± 10 Ma) igneous intrusives extend for ≈1,600 km south of the boundary between the Qiangtang and Songpan/Bayan-Har terraines (Long et al., 2015; Roger et al., 2000), following the Jinsha suture (Figures 6 and 8). Tomographic receiver function data that reveal the existence of a south-dipping velocity anomaly beneath and south of that suture have been interpreted as evidence for a Eurasian plate slab subducted southwards to at least ≈250 km-depth (Kind et al., 2002). This is consistent with the sections proposed by Meyer et al. (1998), Roger et al. (2000), and Tapponnier et al. (2001), and with model Slab 2 in the sections of Figure 6. This is also in keeping with the position of plateau P2, between T2 and T3 (Figures 5 and 7–9), which would match with the Qiangtang high plains, that would presently correspond to the northern half of the oldest, Eocene Tibet plateau (Tapponnier et al., 2001).

Thrusts T4 and T4', that are mostly active between 33 and 14 Ma in the model, mark the northern limits of two more recent model sub-plateaus (P3 and P3') (Figures 5h, 5e, and 9f; Supplementary Animation 3 in Supporting

Figure 9. (a–h) Detailed maps of full kinematic development of faulting in DE model (based on Figures 4a, 4b, 4e, 4g, column six, and Figure 5k). A schematic, first-order correspondence between modeled (a–c) and observed (d–h) SE Asian tectonic features (Figures 2, 3, 7, 8) is proposed. (a–c) outline crustal thickening/thinning, high-resolution faulting, and overall dimensions/offsets/rotations in model. (d, e) show potential correspondence of model faults, uplifted plateaus and extensional regions with large Tertiary Asian tectonic structures. (f–h) display more detailed relationships between observed and model-generated faulting/deformation/kinematics. In (f), colored, curved, dashed lines are DE model's successive south-dipping thrusts (T2 to T6') that bound model sub-plateaus P1 to P5'. More linear lines are main DE model's strike-slip faults (including S1, S2, D1-3, and X1, K1). Light and darker blue DE Modeling regions of extensional stretching correspond to distributed Tertiary extension and rifts/oceanic basins, respectively (North China; South China and Andaman Seas; Indian and West Pacific Ocean and marginal seas) (Figures 1–3 and 8). DE model large, more stable blocks B1, B2 and B3 are interpreted as equivalents of Sunda, South China and North China cratons. Numerous north-trending faults (thrusts or strike-slip) on the right side of the indenter's right corner (and left side of B1) may be compared to those observed across Yunnan and the Shan Plateau (Figures 3 and 5g). Figures 9g, 9h show broad-scale, synthetic model faulting, with eastern, right-lateral faulting pulses (green and blue, respectively), (Supplementary animation 3), superimposed with latest model stage GPS proxy. For optimal comparison with maps in Figures 1, 2, and 8, all this figure frames are rotated clockwise by ≈25°, in keeping with India's present-day GPS convergence relative to Eurasia (Figures 1, 3 and 10b).

Information S1). At this stage, the largest, southern model sub-plateau may be taken to correspond mostly to the Songpan/Bayan-Har high plains, that extend across the width of northern Tibet, mostly south of the Kunlun Range. The model's T4/T4' thrusts would thus mostly represent the main, south-dipping, frontal thrusts that uplifted that range, along the actual northern edge of the ≈4,500 m-high Tibet Plateau, south of the younger, lower (≈3,000 m) Qaidam and fellow basins (Figures 7 and 8). Late Tertiary/Quaternary shortening has long been described across much of these basins, particularly between Ayakkum and Aqqikkol lakes, across the Qiman Tagh range, etc… (e.g., Molnar, Burchfiel, K'uangyi & Ziyun, 1987; Molnar, Burchfiel, Ziyun, et al., 1987; Tapponnier et al., 2001; Tapponnier & Molnar, 1977 ≈8 Ma, Craddock et al., 2011; Liu et al., 2015). The volcanic arc that extends for ≈1,000 km (from ≈78 to ≈92°E) just south of the Kunlun range (Figures 6 and 8) exposes principally andesite/shoshonite and ignimbrite flows with mostly 10 ± 8 Ma ages and including a few post-glacial to historical craters (e.g., Long et al., 2015; Wittlinger et al., 2004). Estimates of cumulative, mostly post ≈10 Ma (e.g., Liu et al., 2015; Z. Li et al., 2021) and Plio-Quaternary shortening between the Kunlun and Qilian ranges reach up to ≈120 km (Métivier et al., 1998; Meyer et al., 1998). Hence, both the volcanism and maximum shortening are consistent with young, likely still ongoing, south-dipping subduction beneath the Kunlun range (Figure 6) down to about 100 km-depth south of the Qaidam (e.g., Figures 15 and 17 in Meyer et al., 1998) and possibly ≈250 km south of the western Tarim (Wittlinger et al., 2004). That northern, well-developed, lithospheric-scale structure may be taken to correspond to Slab 3 in the model sections of Figure 6.

The youngest thrusts in the model (T5 and T6-T6') define the northern boundaries of sub-plateaus P4 and P5-P5', whether south or north of the newly-born left-lateral strike-slip fault S2 (Figures 4, 5, 8, and 9). In model time scale (ms), these structures start forming between ≈20-14 and 6 Ma, from south to north, respectively (Figures 5i–5k). As suggested above, the two youngest model sub-plateaus (P4 and P5) are comparable with the Qaidam and Suhai basins, respectively, while sub-plateau P5', north of S2, might be considered equivalent to the flat-topped Altyn Tagh fault pushup (*ATFPU*, Figures 3 and 7–9; e.g., Mériaux et al., 2012, and references there-in), north of the Altyn Tagh Fault (ATF). In this region, tomographic data show that the Tarim lithosphere can be imaged to subduct southwards to a depth of more than 110 km (Wittlinger et al., 1998). That lithospheric-scale structure, which bounds the edge of Tibet, may thus be matched with the smallest and shallowest Slab 4 in the model sections of Figure 6. Farther eastwards, thrust T6 in the model (Figures 5 and 9) may be readily compared with the active, 600 km-long megathrust that follows the northern front of the Qilian Shan (QLS, Figures 7 and 8), and is the youngest such structure along the northern boundary of the Tibetan Plateau (e.g., Z. Li et al., 2021, 2022, and references therein). That megathrust, which has been seismically imaged to dip ≈40 ± 15° southwards to depths of at least ≈10 km, is generally accepted to be at most 10 to 6 Ma old, and has likely absorbed a minimum of ≈35 km of shortening (e.g., Meyer et al., 1996, 1998; Zheng et al., 2013; Zuza et al., 2016).

In summary, the Discrete Element Model of plateau generation processes described here, which co-involves the northwards-stepping growth of 5 successive sub-plateaus bounded by 5 megathrust systems, is broadly consistent with the Tertiary tectonic history of Tibet based on the growing body of 3D geological evidence (e.g., Tapponnier et al., 2001). It includes the creation of regularly spaced mountain ranges, as also observed in earlier 3D analog modeling attempts (e.g., Davy & Cobbold, 1988). Like all previous models, however, this new DE model critically lacks the effects of fluvial erosion or of its limitation, concurrent with widespread internal drainage within the western two thirds of the plateau (Figure 7), a process bound to increase topographic flatness by the infilling of isolated, captive basins between the spaced ranges (e.g., Liu-Zeng et al., 2008; Métivier et al., 1998).

3.2. Two Main, Northwards Younging, Sinistral Shear Zones, and Many Shorter Conjugate Right-Lateral Faults

Between ≈45 Ma and present (ms), a large fraction of the model's collisional convergence is absorbed by two main left-lateral, ≈NE-striking strike-slip faults (S1 and S2, Figures 4, 5, and 9) that successively nucleate and propagate toward the northeast, isolating two large blocks (B1 and B2). Such dominant, long-lived, far reaching and relatively stable sinistral faulting is accompanied by smaller scale, more distributed and shorter-lived right-lateral faulting within B1 and B2, along the eastern side of the model region facing the indenter (Figures 4, 5, 8, and 9; Supplementary Animation 3 in Supporting Information S1).

3.2.1. Early Mega-Sinistral Faulting: S1, the Ailao Shan-Red River Shear Zone (ASRRF)

As previously described in detail, S1 forms and starts propagating rapidly toward the eastern boundary of model-Asia between 44 and 38 Ma (ms), that is, between ≈10 and 16 Myr after the onset of indentation (Figure 4, third

column, Figures 5d–5f and Supplementary Animation 3 in Supporting Information S1). The total cumulative offset along S1, which remains active and left-lateral until ≈7–8 Ma (ms), reaches up to ∼1,200–1,500 km (Figures 4 and 9). Over a length of ≈5,000 km, S1's average strike is ≈60°NE, at an angle of ≈30° from the indenter front (or 85°NE if the indenter is rotated in a position similar to that of India, Figures 9a–9c). Toward the northeast, S1 veers northwards by ≈23° (to 53°NE from the indenter) for a distance of ≈800–1,000 km (Figure S3a in Supporting Information S1), as it approaches the eastern, free-faced edge of the model (Figures 5f, 5g, and 9). As left-lateral displacement increases with time along S1 with continuing model indentation, and as B1 simultaneously rotates clockwise by up to 16°, the eastern stretch of the fault becomes strongly extensional, opening a large, eastwards broadening crack east of its ≈2,500 km-long western segment that remains predominantly left-lateral (Figures 4, 5, 9, Figure S3a and Supplementary Animation 3 in Supporting Information S1).

In the model, between ≈44 and ≈23 Ma (ms), the sinistral slip-rate along S1 increases gradually from ≈4, to ≈14.8, and up to ≈55.6–61.2 mm/yr (Figures 5d–5h), before decreasing back to ≈41.3 to 42.7 and then ≈24.9–26.1 mm/yr between 23 and 6 Ma (Figures 5h–5j and Supplementary Animation 3 in Supporting Information S1). In ≈30 Ma (between ≈38 and 8 Ma), S1 in the model thus absorbs roughly ≈920 km of convergence, at an average rate of ≈31 mm/yr.

Around ∼6–7 Ma (ms), time of the most radical kinematic change along its eastern stretch (Figures 5j and 5k and Supplementary Animation 3 in Supporting Information S1), the slip sense along S1 reverses to become right-lateral. That change coincides with the rapid development of S2 and the incipient extrusion of block B2. In the last 6 Ma (ms), at an average dextral rate of ≈9 mm/yr, S1 takes up ≈55 km of inverted back-slip between B1 and B2 (Figure 5k and Supplementary Animation 3 in Supporting Information S1).

Within the framework of what is now known about large scale tectonic faulting in southeastern Asia (Figures 1–3 and 8) (Allen et al., 1984; Leloup et al., 1995, 2001; Replumaz & Tapponnier, 2003; Replumaz et al., 2001; Tapponnier et al., 1990: and references there-in), and given the modeling limitations outlined earlier, S1 may clearly be considered the DE model equivalent of the Ailao Shan-Red River Shear zone/Fault (ASRRF), longest left-lateral strike-slip fault system in SE Asia (Figures 2 and 9) (Leloup et al., 1995, 2001; J. Li et al., 2022). The ASRRF system likely extends for a total of ≈4,000 km, from south central Tibet, west of Lhasa, along the entire southwestern margin of the South China Sea, to offshore Brunei (Figures 1, 2, 8, and 9), that is, a length comparable to that of S1 (5,000 km) in the DE model. Like S1, it also marks a sharp boundary between the two largest, more stable Southeast Asian Precambrian blocks, South China and North Sunda, that may thus be readily compared with B1 and B2 in the DEM.

Along that mega-block boundary, the fault perpendicular component of slip switches from shortening in the west to extension and normal faulting in the east, about 1,500 km eastwards along strike in central Yunnan (Figure 2; Leloup et al., 1995; Harrison et al., 1996). Farther southeast, extension becomes predominant in the gulf of Tonkin and into the South China Sea, where the ≈1,100 km-long ridge axis veers northwards, anticlockwise, by 60–90°, a directional swing comparable to, if larger than, that (23°) of S1, about 1,000 km SW of where it reaches B1's eastern boundary (Figures 1, 2, and 9). The total, average sinistral offset along the ASRRF, arguably the largest in the world, is of at least 700 ± 200 km, with a potential maximum, of ≈1,200 ± 500 km, based on paleomagnetic studies (Leloup et al., 1995; Yang & Besse, 1993), hence on order of the maximum offset (1,200–1,500 km) along S1 in the DE model.

The timing of sinistral movement along the shear zone (for at least ≈20 Ma, between ≈35 and 15 Ma) (Leloup et al., 1995; J. Li et al., 2022) is also comparable with that along S1 in the model (on order of ≈30 Ma, from ≈38 to 8 Ma), as is the average left-slip rate (43 mm/yr in the model, vs. ≈35–44 mm/yr along the ASRRF; Briais et al., 1993; Harrison et al., 1996).

Finally, the timing of slip inversion and amount of inverted right-lateral displacement along S1 in the model, perhaps the most remarkable kinematic event in the DEM simulation, which occurs between 8 and 6 Ma (ms) and is followed by ≈55 km of dextral slip at an average rate of ≈9 mm/yr along S1 are in keeping with the maximum right-lateral offset (≈57 km since between ≈12 and 5 Ma, at a rate on order of 4–5 mm/yr) along the presently dextral RRF (Leloup et al., 1995).

3.2.2. Late Mega-Sinistral Faulting: S2, the Altyn Tagh-Haiyuan Fault Zone (ATH)

The other large, younger left-lateral strike-slip fault in the DE model, S2 (Figures 4, 5, 9, and Supplementary Animation 3 in Supporting Information S1), may also be interpreted as a clear equivalent of the second

largest sinistral strike-slip fault of continental Asia, namely the Altyn Tagh-Haiyuan fault zone (ATH) (Figures 2, 3, and 8). Overal, including active sinistral faults to the far-east, in and along the Qinling Shan (e.g., Peltzer et al., 1985), that large fault system (Altyn Tagh-Haiyuan-Qinling Fault) stretches all the way from the Karakorum range (e.g., Tapponnier & Molnar, 1977, 1979; H. Li et al., 2021) to at least the Yellow (East) Sea coast, over a total length on order of at least ≈4,000 km (Figure 2), roughly comparable to that of the ASRRF. That total length is less than that of S2 (≈7,500 km) in the DEM, mostly due to the ≈40° difference in orientation between the two. Other similarities, however, are striking. For instance, between Yecheng (YC) in the west and Jingtai (JT) in the east (Figure 8), over a distance of ≈2,500–3,000 km, the ATH hugs the northern edge of Tibet's high topography (Figures 3 and 8), a length comparable to that (≈2,200–2,500 km) of the western edge of thickened model crust in the DEM (Figure 9).

Timewise, S2 is first observed to briefly nucleate around ≈42 Ma (ms), and to subsequently propagate rapidly in the ≈N30°E direction (at a ≈60° angle from the indenter front, for ≈3,000 km (Figure 5e). Its orientation and curvature, as those of D2, the conjugate dextral fault that propagates northwestwards at the same time (Figure 5e), are consistent with Slip-Line Field Theory predictions (e.g., Tapponnier & Molnar, 1976; Tapponnier et al., 1986). However, in the model, both S2 and D2 stop slipping fairly shortly thereafter (around ≈34 Ma, i.e., ≈8 million years later, Figure 5g, and Supplementary Animation 3 in Supporting Information S1), as S1 takes its long-lasting lead in the eastwards extrusion of B1. During that relatively short, early deformation period, S2 slips at a maximum rate of ≈1.1–1.6 mm/yr (Figure 5c), accumulating only at most ≈13 km of sinistral slip. Nonetheless, such a short pulse of moderate faulting may account for local observations of Eocene deformation along the ATF, particularly west of ≈95°E (Yin and Harrison, 2000).

Later, starting at ≈25 Ma (ms), in the southwest, S2 becomes strongly reactivated and starts propagating northeastwards in several, successive finite steps, the first three of which ≈300 to ≈400 km long, around ≈24 Ma, ≈17 Ma, and ≈14 Ma (ms), (Supplementary Animation 3 in Supporting Information S1). Finally, after ≈6–7 Ma (ms), S2 rapidly reaches the eastern boundary of the model (around 5 Ma –ms-). Simultaneously, as discussed above, sinistral slip along S1 stops and then reverses to dextral. From the SW to the NE tips of the high Tibet plateau in the DEM, finite sinistral offsets across S2 diminish from a maximum of ≈500–600 km, to ≈360 km, and then ≈195 km (Figure 9). This compares fairly well with the eastward decrease of estimated total geological offsets along the GF/ATF between the western Kunlun and Qilian Shan (from ≈500 to ≈180 km and then ≈80 km, Figure 8) (Peltzer & Tapponnier, 1988; Matte et al., 1996; Meyer et al., 1998; Y. Q. Zhang et al., 2001; H. Li et al., 2021). The variable timing of fast motion onset along the ATF in the model is also in keeping with those inferred in the field (≈24 Ma in the west, e.g., H. Li et al., 2021 and references therein; 8 to 15 Ma in the east, e.g., Gaudemer et al., 1995, Lasserre et al., 1999, 2002; Z. Li et al., 2022, and references there-in).

In the last 5 Ma (ms), the northeastern-most stretch of S2 in the model takes up ≈150–180 km of left-lateral displacement between B2 and the stable part of model NE Asia, at an average rate of ≈31–35 mm/yr (Figures 5k and 9). While that rate, which is comparable to those along both S1 and the ASRRF, is similar to the longest term (≈112.7 ± 7.3 ka) maximum slip-rate (≈32.5 ± 3.4 mm/yr) found about midway along the ATF at Sulamu Tagh (Mériaux et al., 2004; ST, Figure 8), it is a factor ≈2 larger than the Holocene rates generally accepted along the central ATH, that range mostly between ≈14 and 8 mm/yr and tend to decrease eastwards between ≈84°E and ≈105°E (e.g.,; Lasserre et al., 1999, 2002; Mériaux et al., 2005, 2012; Ryerson et al., 2006; Liu-Zeng et al., 2008; H. Li et al., 2021; Z. Li et al., 2021). This may partly reflect the fact that left-lateral extrusion along the northern edge of Tibet has also been accommodated by the Kunlun Fault, at a Holocene average rate of ≈11.5 ± 2 mm/yr (Van der woerd et al., 2002).

Like S1, S2 veers counterclockwise near its NE end, from an average strike of 42° from the indenter's front along its ≈2,500 km-long middle-eastern stretch to a more northerly direction (58° from the indenter's front) along its ≈1,000 km-long, north-easternmost segment (a ≈15° swing, Figure 9c). As block B2 rotates clockwise by ≈1–2° (Figures 5 and 9) (Y. Q. Zhang et al., 1998), the eastern, ≈3,500 km-long stretch of S2 exhibits significant extension, which generates a step by step, eastwards-broadening crack with up to ≈150 km of separation (Figure 9). As discussed below, such an amount of extension may be considered to be roughly in keeping with that observed across the active rifts of Northeast China (Figures 1, 2, and 8) since the Mid-Miocene (e.g., Shi et al., 2020).

3.2.3. Smaller Left-Lateral, Tibetan Strike-Slip Faults

At a more detailed level, smaller left-lateral strike-slip faults appear to be generated by the convergence of the model's Indian indenter into model Asia (Figure 9 and Supplementary Animation 3 in Supporting Information S1).

They are difficult to identify and delineate precisely because their total offsets (≤100 km in the DEM) are near the lower limit of what is detectable given the size (≈50 km) of the model's elements. Also, they are shorter than S1 and S2, and two of them affect mostly the highly deformed interior of the DEM's "Tibet" plateau (Figures 9c–9h). One of these faults is the short lived S3, northwest of S2 (Figure 5j). Another is S1.1, southwestern branch of S1 (Figures 5h–5k), that apparently forms between 36 and 27 Ma (ms). At a very speculative level, we infer that S1.1 may be compared to the left-lateral Damxung fault (along Nianqingtangula's SE front; Armijo et al., 1989; Wu et al., 1990; K. Li et al., 2022) and to part of the westernmost stretch of the early Jiali fault system, north of Lhasa.

Two other significant sinistral faults (dubbed K1 and X1 on Figure 9) are discernible within the central part of the DEM plateau, and appear to cross its eastern margin (Figure 9). We propose that they might be interpreted to be model analogs of the Kunlun and Xianshuihe Faults (KLF and XSF, Figure 9d) respectively, whose measurable maximum finite offsets (of the Yellow and Jinsha rivers, east of Maqen and Yushu, respectively) are only on order of ≈80 ± 10 km (e.g., Chevalier et al., 2017; Ding et al., 2004; Gaudemer et al., 1989; Vanderwoerd et al., 2002), hence roughly commensurate with twice the average size of the model elements. Such offsets are so small in the model, however, that this interpretation remains tentative.

3.2.4. Dextral Strike-Slip Faulting East and South of the Tibet Plateau

Along the eastern side of the DEM's indenter and "Tibet" plateau, a substantial part of the deformation is accommodated by NNW to NE striking, right-lateral strike-slip faults (e.g., D1-D4 in Figures 4 and 5, and Figure 9). In the model, these faults, which, on a broad scale, may be considered "conjugate" of the generally longer left-lateral ones, nucleate and grow to maximum length of ≈1,000–1,800 km, from almost the beginning (≈53 Ma, -ms-) to the end (≈5 to 0 Ma, -ms-) of the collision indentation process (Supplementary Animation 3 in Supporting Information S1). They first form across the western corner of B1 (5 main branches), then within that of B2 (also 5 branches), and slip mostly during two distinct, successive periods, between 45 and 33 Ma (12 Mys, -ms-), and 16 and 4 Ma (12 Mys also, -ms-) (Figures 4, 5, 9 and Supplementary Animation 3 in Supporting Information S1). Such dual episodes of growth/slip coincide roughly with the 2 rapid phases of propagation of S1 and S2 toward the DEM's eastern boundary (Supplementary Animation 3 in Supporting Information S1). Correlatively, within each block, these dextral ("D") faults tend to nucleate and develop successively from the southwest to the northeast (Supplementary Animation 3 in Supporting Information S1). Some of the most recent "D" faults also tend to reactivate the formerly abandoned, farthest north-reaching branches of the earlier ones (Figure 5). The westernmost "D" faults (D0, D1.1, and D2, Figures 5 and 9) take up the largest dextral offsets.

We interpret the model's dextral SE- to SSW-striking faults across the western corner of B1 (Figures 4, 5 and 9) to be comparable with the sub-parallel, now inverted, mostly SW-striking strike-slip faults that cross the Shan Plateau (Figures 3 and 8), and include, from east to west, the particularly large Dien Bien Phu, Gaoligong, Sagaing and Jiali Po-Cu Faults (DBF, GGF, SGF, and JLPF, respectively, in Figure 8) as well as numerous other smaller, inverted, dextral faults across Yunnan/Myanmar (e.g., Le Dain et al., 1984; Lacassin et al., 1997, 1998; Shi et al., 2018; Y. Wang et al., 2014).

Similarly, on the east side of block B2's model plateau margin, we interpret the NW to NE striking dextral faults (Figures 4, 5 and 9) to be kinematically similar to long recognized faults/shear zones with clear dextral slip components on both sides of the Sichuan basin, namely the Huaying Shan Shear Zone (HYF) (T. Li et al., 2021), the Longmen Shan's Wenchuan (e.g., Wu et al., 2014; Xu et al., 2009) and Qingchuan faults (LMS, QCF) (e.g., Tian & Lin, 2021), the Longriba faults (LRBF) (e.g., Ren et al., 2013), and farther north in western Gansu and eastern Qinghai provinces, the Wenquan and Haiyen faults (WQF, HYF) (e.g., Meyer et al., 1998; Van Der Woerd et al., 2002; also called Ela Shan and Riyue Shan faults in Yuan et al., 2011) (Figures 3 and 8). The latter two faults are now estimated to have slipped at rates on order of ≈0.8–1.6 mm/yr since the late Miocene (Tortonian), and to have maximum offsets on order of 9–12 km (Yuan et al., 2011).

Note that dextral faulting along D0, which first hugs the indenter front and then swings almost orthogonally southwards along the westernmost edge of B1, largely accommodating the right-lateral decoupling between model India's rigid indenter and model Asia, is particularly complex (Figures 5 and 9, Figures S3a–S3c, and Supplementary Animation 3 in Supporting Information S1). Such complexity is comparable to that of dextral faulting across southern Tibet and westernmost Sunda which, from far west to far east, co-involves the Karakorum Fault (KAF, Chevallier et al., 2005, 2012, 2015; H. Li et al., 2021), segments of reactivated faults along and between the western Zangbo and Bangong sutures (YZS, BNS) (e.g., Murphy et al., 2010; Taylor et al., 2003),

the Gyaring Co and Beng Co faults (e.g., Armijo et al., 1989; K. Li et al., 2022; D. Wang et al., 2021), and finally the Jiali Po-Cu and Sagaing faults (JLPF and SGF) (e.g., Li Y. et al., 2020; Wang H. et al., 2020), as it also takes an orthogonal turn (≈90° southwards) around the East Himalayan Syntaxis (Figure 8) (e.g., Armijo et al., 1989; Coudurier-Curveur et al., 2020; Tapponnier et al., 2001).

In the DE model, movement along D0 is further affected by the rotation of block B1 (Figure 9). Along the indenter front, between ≈40 Ma and present (ms), slip occurs at a variable rate of between ≈2 and 25 mm/yr (≈10–15 mm/yr, (ms), on average), which corresponds to ≈400–600 km of total dextral slip (Supplementary Animation 3 in Supporting Information S1). During the same 40 Ma (ms), along the nearly NS-striking, east-side of the indenter, D0 takes up as much as ≈1,700 km of right-lateral extrusion between model India and block B1 (model Sunda), at an average rate of ≈42.5 mm/yr (Figures 5 and 9, Figures S3 and S4 in Supporting Information S1). Farther southeastwards, dextral slip along the ≈ southeast-striking southern edge of B1 becomes slower again, with an average rate of ≈15 mm/yr (≈600 km in the last ≈40 Ma, -ms-), in keeping with the fairly large (≈16°) clockwise rotation of B1, that partly counteracts the extrusion of its southeast corner (Figure S3 in Supporting Information S1).

During the entire collision span (≈54 Ma), the total strike-slip displacement along the east side of India, between the Assam plain and the northern tip of Sumatra, may have reached ≈2,300 km, implying an average dextral rate of ≈42 mm/yr. That movement occurred mostly near the western edge of Sunda, along the Shan Plateau scarp, Sagaing and related fault splays (Figures 1–3, 8 and Figures S3 and S4 in Supporting Information S1). In the final stage of the DE model, only ≈1,700 km separate the northeast tip of the indenter from the southwest tip of B1 (Supplementary Figure S3a in Supporting Information S1), consistent with an average rate of ≈32 mm/yr. The present GPS displacement rate along Sunda's western boundary, in the average N10°E direction, is on order of 35–36 mm/yr (including 18–20 mm/yr across the Sagaing Fault) (Socquet et al., 2006). Overall, there is thus fair kinematic agreement between the observed, long and short term, displacement rates and amounts along the east sides of India and of the DEM indenter.

Additionally, farther southeast, along much of the length of the ≈N140°E-striking Sumatran Fault, the most recent GPS data (Bradley et al., 2016) are consistent with a dextral slip-rate of 14.5 ± 0.5 to 16 ± 5 mm/yr, hence roughly in keeping with that (≈15 mm/yr) generated by the DEM.

3.3. Three Large Rifts Evolving Into Oceanic Basins to Separate Sunda From India, and South China From Sunda and North China

The deformation induced by the indenter's penetration into the DEM is radically different north of the collision front and far from it (Figures 4, 5, 8, 9, and Supplementary Animation 3 in Supporting Information S1). While crustal shortening and thickening play a leading role in front of the indenter, extensional “cracking” (rifting) and ultimately wholesale separation (spreading) predominate away from it. As long recognized, this radical change in broad-scale deformation is a simple consequence of torsion (Peltzer & Tapponnier, 1988; Tapponnier et al., 1986), due to the contrast between the indenter's strong push on one side of the model and the weaker resistance along its other, “freer” sides.

The unobstructed growth of S1, which leads to the large, unbounded extrusion of B1, co-involves a clockwise rotation that splits and separates it from both model Asia on one side, and model India on the other. Block B1 thus cracks away from them, which results in the opening of broadening triangular gaps (Figures 4, 5, 8, 9, Figures S3 and S4, and Supplementary Animation 3 in Supporting Information S1).

3.3.1. Andaman Sea and Mergui Basin

In the model, the first signs of extension between B1 and the Indian indenter start around 44 Ma (ms), as D1.1, and then D0 are activated near B1's southwest corner (Figure 5 and Supplementary Animation 3 in Supporting Information S1).

In SE Asia, such extension, coupled with dextral strike-slip faulting, may be taken to correspond to the initial opening of the Mergui basin, at the southern tip of the Ranong/Khlong-Marui strike-slip fault zone, along which there is now clear evidence for metamorphic dextral shear in the Middle-Eocene (Ar/Ar cooling ages between 45 and 37 Ma, Watkinson et al., 2011), starting soon after the collision onset (≈50–54 Ma). That shear would have heralded the birth of the wedge-shaped, greater Andaman basin, whose maximum ≈NS length, and

≈EW width between the western edge of Sundaland and the Andaman-Nicobar Arc, now reach ≈1,200 km and 550 km, respectively (Figures 1, 2, 4, 5 and 9). The complete opening of that basin, mostly as a composite, dextral pull-apart, likely co-involved successive strike-slip shear along initially the Shan Plateau scarp and later the Sagaing fault. In the model, a little over half of the basin (≈800 km ≈ NS × 300 km ≈ EW) opens as a crack between ≈44 and ≈25 Ma (in ≈19 Ma, (ms) (Figures 1, 2, 4, 5, 9 and Figure S3c in Supporting Information S1). This is also roughly in keeping with a convergence rate on order of ≈4 cm/yr (≈4.2 cm/yr).

The remaining part of the model's "Andaman" basin continues to open between 24 Ma (ms) and present, as a result of dextral shear along the model's India/Sunda boundary. During that stage, the DEM north-south length and east-west width of the basin increases by about 400 and 180 km (to 1,200 and 480 km), respectively (Figure S3c in Supporting Information S1). Such a length for the post Miocene to present, central part of the mid-Andaman basin is roughly consistent with that (≈440 ± 30 km) obtained by assuming that the present GPS slip-rate along the Sagaing fault (19 ± 1 mm/yr) (Socquet et al., 2006) remained nearly constant during the last 23 Ma.

Overall, most of the broad-scale geometric and kinematic results of the DEM model–notwithstanding its simplicity–are thus fairly consistent with the currently known Early Tertiary to present geological and tectonic history of the region separating the northeastern tip of India from the northwestern corner of Sunda (Figures 1 and 2) (Curray, 2005; Curray & Moore, 1974; Curray et al., 1979; Peltzer & Tapponnier, 1988; Morley, 2012, Figure 2; and references therein; Srisuriyon & Morley, 2014).

3.3.2. South China (Nan Hai) Sea

In the DEM, the large left-lateral shear zone S1 reaches the eastern boundary of the model between 37 and 36 Ma (ms). This immediately fosters cracking inside model Asia, mostly along S1. From west to east, step by step, such en echelon cracking widens the separation between blocks B1 and B2 (Figures 4, 5, 8, 9, Supplementary Animation 3, Figures S3 and S4 in Supporting Information S1). The resulting opening continues nearly unabated until ≈8–9 Ma (ms), as long as S1 remains left-lateral (Figure 5, Supplementary Animation 3 in Supporting Information S1). As S1 steps northwards and veers anticlockwise by up to ≈23°, in a more northerly direction, starting ≈1,000 km west of the DEM eastern boundary, the separation between B1 and B2 increases greatly (Figure 9). Over that northeast stretch of ≈1000 km, its width broadens northeastwards from ≈800 km to ≈1,300 km (Figure 9 and Figure S3 in Supporting Information S1).

Such overall dimensions are comparable to those of the deepest part of the South China Sea basin, which is at least ≈900 km and at most ≈1,300 km wide (along NNW-SSE striking sections between Hainan and Sabah), and whose ≈NE- trending axis is about 1,100 km long (Figures 1 and 2) (Briais et al., 1993). Like the partly triangular, open gap between B1 and B2 at the eastern end of S1 in the model (Figures 4, 5, 9, and Figures S3a and S4 in Supporting Information S1), the area floored by oceanic crust with well dated magnetic anomalies in the central South China Sea broadens northeastwards in a roughly triangular way (Briais et al., 1993) (Figures 1 and 2), an overall, robust structural pattern that remains undisputed in all recent studies (e.g., Barckhausen & Roeser, 2004; C. Li et al., 2015; Sibuet et al., 2016). Note, however, that the maximum dimensions of the recognizable oceanic seafloor (≈650 km wide by ≈740 km long) are significantly less than those of the deep South China Sea basin, which remains poorly understood, and suggest larger amounts of Early Eocene extension between Borneo and South China.

The ages of the dated South China Sea seafloor (anomalies 11 to 5, Briais et al., 1993) implies unabated spreading between at least ≈33 Ma and ≈15 Ma (a time period of ≈18 Ma), which is roughly in keeping (though briefer by ≈9 Ma) with the duration of extension (≈36 Ma to 9 Ma, ≈27 Ma –ms-) between B2 and B1 in the DE Model. Although fairly fast, the rate of spreading consistent with the South China Sea magnetic isochrons (which decreases with time from ≈5 to ≈3.5 mm/yr, 4 ± 1 mm/yr on average, Briais et al., 1993), is also commensurate with the rates of separation between B1 and B2 in the DE model, that decrease from ≈61.2–55.6 mm/yr (≈58 mm/yr on average) down to ≈21–26 mm/yr (≈23.5 mm/yr on average) between 33 and 23 Ma and 23 to 6 Ma (ms), respectively, consistent with an overall, average rate of ≈4.1 mm/yr.

3.3.3. North China peri-Ordos Rifts (Yinchuan/Weihe/Shanxi Grabens), and Hebei Plain

In the Discrete Element Model's final few millions of years (≈8 Ma, -ms-), fairly rapid extension occurs along the ≈3,500 km-long northern stretch of left-lateral fault S2, and starts physically separating block B2 from block B3 (Figures 4, 5, and 9; Supplementary Animation 3 in Supporting Information S1). The largest amount of separation (≈ EW (≈N115°E) opening, or "rifting") between B2 and B3 in the model (≈100–150 km) is observed along

the more northerly striking (≈N58° from indenter), ≈1,000 km-long, easternmost stretch of S2 (Figures 4, 5, 9 and Supplementary Animation 3 in Supporting Information S1).

While it might seem straightforward to compare that B2/B3 lateral extension to the rifting observed across northeast China between the Gobi desert and the Shandong peninsula, a region also about ≈1,000 × 1,000 km-wide (Figures 1 and 2), however, the strongest extensional deformation across that region has apparently been going on for much longer than 8 Ma (ms) (at least since the Miocene, ≈20 Ma) (e.g., Shi et al., 2020). Besides, it has co-involved several, almost orthogonal, ≈NS and ≈EW rifts (Yinchuan, Hetan, Weihe, Shanxi, and Hebei plain; Figures 1–3 and 8), spaced by hundreds of kilometers, and whose oblique bounding faults slip at recent rates of only a few mm/yr, slower than the overall DEM rate (≈5–18 mm/yr on average), likely due in part to additional, large scale, CCW block rotation (e.g., Briais et al., 1993; Hao et al., 2020; Middleton et al., 2016; Tapponnier & Molnar, 1977; Y. G. Zhang et al., 2018).

One plausible reason for the complexity of Late Cenozoic extension across northeast China may be that the direct, northeastwards propagation of sinistral shear along the Altyn Tagh/Haiyuan and Kunlun/Tianshui strike-slip faults (Figures 3 and 8) has been partly hampered (e.g., Cheng et al., 2021) by the strength, hence resistance, of the large Proterozoic to Archean blocks, including the up to ≈2.7 Ga-old Ordos and Alxa cratons (e.g., Kusky et al., 2007; W. R. Wang et al., 2019; Zhao and Zhai, 2013; and references therein), that make the bulk of the North China/South China lithospheric assemblages hard to rupture through.

4. Regional Block Rotations and Paleo-Latitude Changes

Across much of southeast Asia, the Indian collision has produced large changes in the positions and orientations of Cretaceous and early Tertiary rocks. Such movements, which still co-involve mostly NNE to ESE translations, with additional clockwise rotations (e.g., Avouac & Tapponnier, 1993), are particularly clear on the present-day, continent-scale, GPS displacement field (e.g., Gan et al., 2007; Wang & Shen, 2019; W. Wang et al., 2017) (Figures 3 and 10), as well as in the DEM results (e.g., Figures 9e–9h and Supplementary Figure S5a–S5d in Supporting Information S1) and animations (Supplementary Animation 1–3 in Supporting Information S1). The distribution of somewhat more ancient (including Early/Mid Mesozoic) regional displacements has also been broadly explored by many paleomagnetic research groups during the past four decades (e.g., Achache et al., 1983; Chen et al., 1993; Enkin et al., 1992; Gilder et al., 1993; Huang & Opdyke, 2015; S. Li et al., 2017; Otofuji et al., 1990, 2010, 2012; Yang & Besse, 1993, 2001; Z. Yang et al., 1995, 2001; Van Hinsbergen et al., 2011; Yamashita et al., 2011).

Here we compare, to a first order, the DEM's final stage rotations and latitudes predictions (Figures 4f, 4d, and 5, 9–11) with the data published and discussed in the papers listed above, and more specifically in the synthetic overviews of S. Li et al. (2017) (Figure 10a and Figure S6 in Supporting Information S1) and Chen et al. (1993) (Figure 11a).

The largest finite rotations predicted by the DE model are observed near the southeast and northwest sides of the indenter (Figure 10c). While data within the highest, northwest part of the Tibet plateau is still too sparse for a critical assessment, the paleomagnetic declination measurements across South China, Sichuan, Yunnan, and Sunda, recently compiled and discussed by S. Li et al. (2017) are sufficient to warrant close examination. In our appraisal of this data (Figure 10 and Figure S6 in Supporting Information S1; after Figures 3 and 4 in S. Li et al., 2017), we discard measurements with extreme local variations or that are located on large faults, values derived from young volcanic rocks, as well as most of the data along the highly sheared western boundary of Sundaland. Figure 10a thus includes only ≈75% of the Li et al., 2017's data set.

The largest finite rotations (averaging between ≈40 and 69° clockwise, Figures 10a and 10b) are observed south of the Ailao Shan, in the Lanping and Simao basins, where late Cretaceous red beds are strongly folded (e.g., Leloup et al., 1995), and where "zipper tectonics" along the ASRR shear zone switches from shortening west of Midu (Figure 3) to extension farther east (Harrison et al., 1996; Leloup et al., 2001). To the south, across eastern Sundaland, the declination rotations are less (≈27° on average), but remain dominantly clockwise and rather uniform, consistent with fairly rigid block behavior (Figures 10a and 10b). Toward the north (Chuandian basin, S. Li et al., 2017), between the Red River and Xiaojiang faults, average clockwise rotations also decrease to ≈23° (Figures 10a and 10b). Yet farther north, across most of southeastern China, smaller, fairly uniform finite rotations (≈12° on average) clearly attest to broad continental block rotation in the Tertiary. In general,

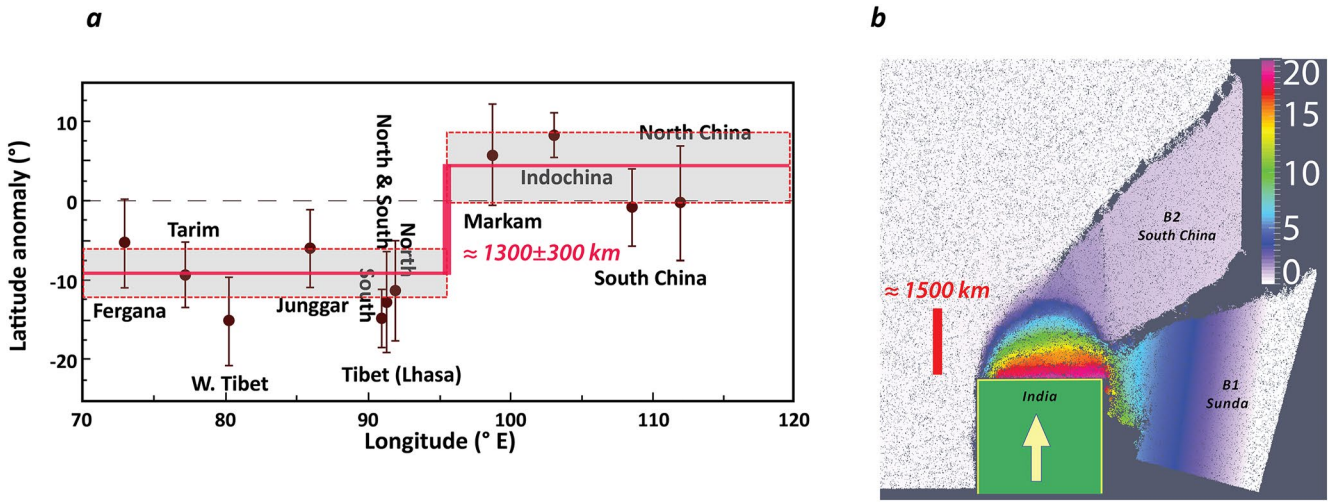

Figure 11. Paleomagnetic inclinations (Paleo-latitude) discrepancies across southeast Asia. (a) Post Cretaceous Paleo-latitude differences between Tibet and Sunda/South China (after Chen et al., 1993, Figure 7; see also Huang & Opdyke, 1992, 1993, and additional references in text) range mostly between ≈1,000 and 2,000 km (≈1,300 ± 600 km on average). (b) Predicted DE modeling inclination difference (Figures 4f, six column) between South Tibet and Northern Sunda is ≈1,500 km. Note relative latitudinal stability of block B1, in spite of large extrusion displacement.

most of these results are in keeping with previous interpretations, particularly those long advocated by Yang and Besse (1993, 2001) and Z. Yang et al. (1995, 2001).

Overall, in a semi-quantitative way, the block rotations generated by the DE modeling are thus in fair agreement with the broad-scale declination data distribution summarized above (Figure 10c). The main clockwise rotation senses, distribution, and relative amounts in the model are, perhaps not surprisingly, similar to those observed. In general, however, the model rotation values are smaller. This is particularly clear for the finite rotations of blocks B1 and B2 (Figure 10), that are about 10° less than those now fairly well constrained across Sunda and South China. We infer that this difference is related to the other main discrepancy between the DE model results and the observed Asian deformation, namely the overall orientations of the main left-lateral faults S1 and S2, that strike up to ≈30–40° more northerly than do the Red River and Altyn Tagh-Haiyuan Faults (Figures 8 and 9).

Measuring Paleo-latitudinal changes across Asia, a fundamental goal of geophysical research since the onset of Plate Tectonics, has been key to quantify the amounts and rates of convergence between India and other Asian blocks, both before and during the collision.

Early work focused on assessing the latitudinal position of final continental impact along the Zangbo suture (e.g., Achache et al., 1983), in order to constrain the amount of post-collisional shortening across both India and Asia. That impact was found to have occurred at ≈10° North, implying ≈2,200–2,500 km of total continental shortening. The now robustly corroborated smaller bound for such shortening (e.g., Molnar & Stock, 2009) was thus used as a basis in the DE modeling presented in Figures 4 and 5.

Posterior work focused on post-Jurassic/Cretaceous paleomagnetic constraints on a broader scale, across much of SE Asia (e.g., Chen et al., 1993, refs. therein, and more recent work quoted above).

Beyond corroborating a collision impact at ≈5–10°N (Chen et al., 1993, Figure 8), the Paleo-latitude anomaly data indicated that most south Tibetan sub-regions, from west to east, had moved northwards relative to China and Indochina by up to ≈1,300 ± 300 km (Chen et al., 1993, Figure 7; and Figure 11a). This is in keeping with the DE modeling results shown in Figures 4f and 11b, where the post-collision latitude difference between southern Tibet and South China/Sunda reaches up to ≈1,500 km, while the paleo-latitudes of the latter two rotating blocks vary little, a long puzzling observation sometimes used to challenge the occurrence of continental extrusion in SE Asia.

5. Wavering Between Dominant Mountain Building and Strike-Slip Faulting

For much of the indentation span, the deformation of the Tibetan highlands co-involved both crustal-thickening/mountain-building and strike-slip faulting (Figures 3–9). How these two main deformation

regimes interacted quantitatively, and whether one or the other predominated at any given time during the ≈54 Ma-long collision process is to be clarified.

To better elucidate this question, we recorded 361 "moments" (each 0.15 Ma long) during the entire DE modeling evolution, in order to quantify, step by step, the volume change during indentation (Figures 12a and 12b, Figures S7a and S7b and S8 in Supporting Information S1). From the temporal pattern of vertical deformation in the stepwise distribution derived directly from the indentation data (Figure 12a), we calculated, using both Fourier transform (Figure 12b) and Wavelet analysis (Figures S7a and S7b in Supporting Information S1), the power spectra of crustal thickening changes at 4 different filtering time-periods. The 4 spectral envelopes corresponding to periods of 2.6–54 Ma, 13.9–54 Ma, 6.9–13.9 Ma, and 3.7–5 Ma are plotted as smooth red, blue, green and violet curves in Figure 12 and Figure S7 in Supporting Information S1.

This enables to visualize how bulk vertical and horizontal deformations may oscillate during the DE Modeling, and whether potential swings might correspond to distinct deformation events in Tibet/Asia, north of India.

The blue, long "period" curves in Figure 12b and Figure S7b in Supporting Information S1 broadly show two main, fairly "smooth", convex-upwards phases culminating in maximum thickening between ≈52–38 Ma and 22–5 Ma, respectively. Both terminate with two steep drops that herald the birth and rapid growth of the two largest sinistral faults S1 and S2, between ≈43–37 Ma, and ≈9–4 ka, respectively. Note that the model epoch during which S1 is most active (≈40 to ≈10 Ma –ms-) encompasses the 35-15 Ma of metamorphic sinistral shear along the Ailao-Shan Red-River zone (e.g., Leloup et al., 1995, 2001) (Figure 12b and Figure S7b in Supporting Information S1). On the other hand, the shorter model epoch during which S2 slips (≈9 Ma to present) corresponds to less than half the time (24 Ma to present) during which the Altyn Tagh/Lenglonglin/Haiyuan Fault zone is inferred to have been active as it grew toward the northeast (e.g., Gaudemer et al., 1995; H. Li et al., 2021; Mériaux et al., 2004, 2005, 2012; Ryerson et al., 2006).

At a more speculative level, the two shorter "periods" (green and purple curves) may be taken to outline the briefer Tibetan episodes of dominant, local thrusting that thickened the plateau's crust between 55 Ma and present (Figure 12b and Figure S7b, and Supplementary Animation 3 in Supporting Information S1). The yellow arrows (Figures S7a and S7b in Supporting Information S1) that correspond to the onset of thrusts T1 to T6 in the DEM (Figures 4 and 5, Supplementary Animation 3 and Figure S3 in Supporting Information S1) may be taken to roughly coincide with the short period maxima of crustal thickening outlined in Figure 12 and Figure S7 in Supporting Information S1. Note also that the relative hiatus of crustal thickening between ≈32 and 22 Ma (-ms-) (light yellow shaded rectangle in Figure S7a in Supporting Information S1), nearly corresponds to the period of fastest, early seafloor spreading in the South China Sea (Briais et al., 1993, Figure 12a).

In short, the DEM results do suggest that simple swaps between dominant crustal faulting modes in Tibet can orchestrate broad-scale wavering in the continental scale accommodation of an otherwise constant indentation process.

6. Discussion and Conclusions

Although there are noticeable differences between the modeling results presented here and the Cenozoic geologic/tectonic objects and events observed in SE Asia, the DE model produces a majority of features closely comparable to the large Tertiary mountain-ranges, faults, basins, and extensional-rifts that characterize the Eocene to present deformation of the southeastern corner of the Asian continent.

In general, even though it has long been known that the pre-Tertiary history of Tibetan accretion and deformation was multi-phased and complex (e.g., Allegre et al., 1984; Chang & Zheng, 1973; Chang et al., 1986; Matte et al., 1996; Meyer et al., 1998; and references therein), the similarities between the main mountains and crustal structures created by our simple, homogeneous, scaled DE model and those observed or inferred in and around Tibet are striking.

Across the Tibetan plateau, north of the Zangbo suture, the present-day highest topography and post-Paleogene folding/thrusting are mostly aligned along five to six distinct ranges: from south to north, the Gangdese, Bangong, Tanggula/Fenguo, Kunlun, and Qilian ranges (Figures 6 and 7 and Supplementary Animations in Supporting Information S1). Although several of the mountain ranges that cut across the plateau had a protracted tectonic history, with some of them clearly following Mesozoic/Paleozoic sutures (e.g., Kunlun, Qilian Shan), their

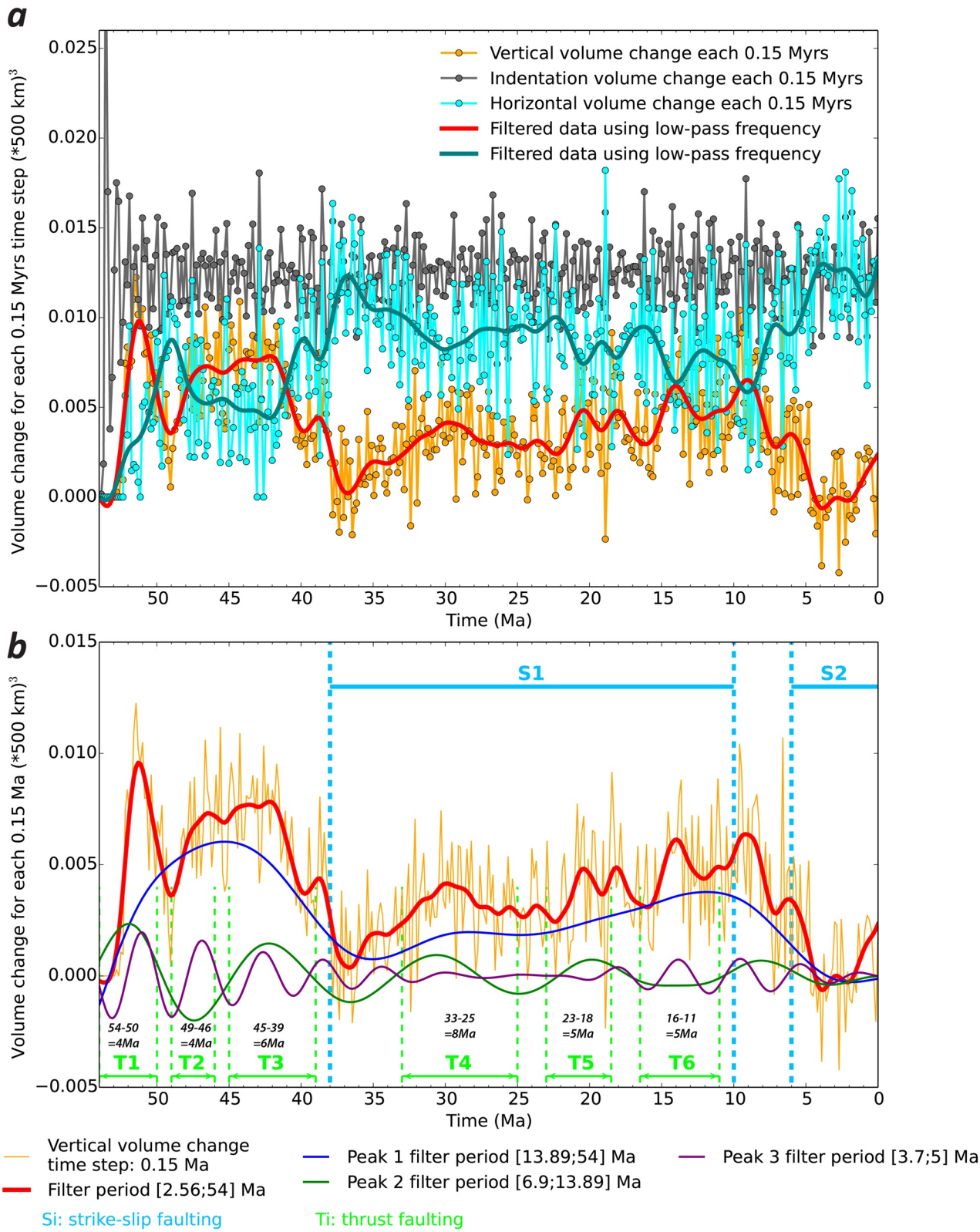

Figure 12.

maximum altitudes (≥6,000 m), recently folded/thrusted boundaries, and exhumation histories imply Cenozoic uplift unrelated to post early-Miocene extension.

Specifically, while Eocene to early Oligocene thrusting is observed in and along the Gangdese range (e.g., Schärer et al., 1984, 1986; Tapponnier et al., 1981, 2001; Yin et al., 1994; and references there-in), more recent, Oligo-Miocene shortening has raised the ranges of central Tibet, while yet younger, Late Miocene to Plio-Quaternary thrusting is still uplifting the Kunlun, Qilian and adjacent mountains (e.g., Meyer et al., 1998; Z. Li et al., 2021, 2022; Liu et al., 2015, and references there-in).

Not only does the DE-modeling create, in sequence toward the north, the 5/6, ≈EW-trending ranges that cross the Tibet plateau from west to east, but it also shows how they end up isolating the flat, ≈EW elongated basins in between, which have long been interpreted as, and dubbed, "bathtub" basins (Liu-Zeng et al., 2008; Meyer et al., 1998; Métivier et al., 1998; Tapponnier et al., 2001, and references there-in).

The model also generates the two largest left-lateral strike-slip fault systems that sever entirely the southeastern corner of the Asian continent (ASRR-RRF, and ATF-HF, Figures 2, 8, and 9). Additionally, it generates the mostly smaller, shorter-lived right-lateral faults that cut the western side of northern Sunda and parts of regions along the edges of eastern Tibet (Figures 8 and 9).

It shows the interactions of the two largest faults/shear zones with both thrusting in the west and extension in the east. And it illuminates, in 3D, the formation of several south-dipping, lithospheric subduction zones beneath the ranges of central and northern Tibet, a few of which now adumbrated by seismic tomography (e.g., Kind et al., 2002; Tilmann et al., 2003; Wittlinger et al., 1998, 2004).

At fairly detailed scales in space (≈50–100 km) and time (≈1 Myr), the 3D simulations/animations help analyze growing "mega-cracks" distributions, faulting across vertical sections, kinematic variations along east-west or north-south directions, as well as progressive latitudinal displacements and rotations. Beyond the identification of thrusts, strike-slip faults and rifts in map view, the model helps depict in section the variations of the maximum and average thickness of the deformed lithosphere beneath Tibet (Figure 6).

The timing of an oscillating balance between crustal thickening and strike-slip extrusion can also be reconstructed. In general, the time-dependent plateau generation process in the DE model matches the geological evidence for stepwise, northwards rise and growth of the Tibetan Plateau (Meyer et al., 1998; Tapponnier et al., 2001) (Figure 6). The overall arrangement and sizes of the main strike-slip faults, as well as their total offsets and along-strike slip-rate variations in and around the plateau in the model are broadly consistent with observations.

Perhaps most remarkably, and unlike any other extant model of large-scale faulting across east Asia, the DEM generates slip-inversion, from left to right lateral, along the boundary (S1) between B1 and B2, as observed between Sunda and South China along the Red River Fault, and this at a time (≈5–6 Ma to present) in good agreement with geological evidence (e.g., Allen et al., 1984; Leloup et al., 1995, 2001, and references there-in).

Finally, as those of Sunda and South China, the rotations of B1 and B2 in the DE model induce along-strike, west to east transitions from fault-perpendicular shortening to fault-perpendicular extension. Along the eastern ASRR shear zone, such extension is known to have driven progressive exhumation of the high-grade Ailao Shan range gneisses, an observation interpreted, based on the regular, westwards younging of Ar/Ar cooling ages along the range's normal faulted northeastern front, to reflect "Zipper Tectonics" (Harrison et al., 1996). Such "zipper" exhumation results from the fact that the rotation of Sunda relative to South China followed a small circle that was more convex northwards than is the ASRR block boundary (Leloup et al., 2001). Even though the DE model

Figure 12. (a) Vertical and horizontal volume changes during 55 Ma-long DE model deformation. Indentation volume changes and vertical/horizontal deformation changes are based on 361 recorded modeling moments (0.15 apart). Two successive moment intervals correspond to 2000 model time-steps and a total of 0.15 million years. The method to calculate volume change is shown in Figure S9 in Supporting Information S1. The indentation volume change (black dots/lines) during each interval represents the volume of all spherical elements in the indentation zone during the period separating M1 from M2 (Figure S9 in Supporting Information S1). This volume change is generally constant, since the indentation rate is a steady input parameter. During that same interval, the vertical volume change (orange dots and red average line) represents the volume of all spherical elements that are pushed up or down, from top to bottom of the model (cross-section view), (Figure S9 in Supporting Information S1). The indentation volume is thus transformed into both vertical deformation (thrusting/thickening) and horizontal displacements (strike-slip faulting). Since the total indentation volume is the sum of the vertical and horizontal deformation, that absorbed by horizontal strike-slip (cyan dots) is the difference between the total indentation and thickening volumes (Blue-green average line). Note particularly large drops in vertical volume change between ≈42 and ≈37 Ma, and between ≈9 and ≈4 Ma. (b) Fourier transform analysis of alternating strike-slip faulting and thrusting/thickening across Tibet and adjacent regions during 55 Ma-long shortening of Asia by the Indian collision. See discussion in text.

is planar, the regular, westwards decrease in extension along S1 (e.g., Figure 9) is in keeping with the Zipper extension process documented along the Ailao Shan.

In short therefore, the DE modeling approach succeeds in producing most of the outstanding tectonic features and events that characterized the deformation of east Asia since the Indian collision began, ≈55 Ma ago. Unlike the early plasticine models (e.g., Peltzer & Tapponnier, 1988), the DEM generates a realistic Tibet plateau with several ranges isolating high-altitude basins, which were not created by variants of numerical, thin-viscous-sheet types models (e.g., Cook & Royden, 2008; England & Houseman, 1986), but do resemble the mega-folds produced by other, early analog models (e.g., Davy & Cobbold, 1988).

Without pre-introduced rheological boundaries inside model Asia, the DEM generates both two continent-scale and many smaller strike-slip faults that compare favorably with the two dominant, left-lateral and subordinate right-lateral faults of SE Asia. Similar faults are either not generated at all, or not where actually observed, by other analog or numerical models (e.g., Davy & Cobbold, 1988; England & Houseman, 1986; Houseman & England, 1986; Schellart et al., 2019; Sternai et al., 2014, 2016).

Last but not least, the DEM engenders both relatively narrow (km to tens of km wide) cracks, and very large (hundreds of km wide) extensional gaps that coincide roughly, geographically and kinematically, with the Tertiary rifts and marginal oceanic basins observed within and around SE Asia (Figures 1, 2, 8 and 9). This is also in contradiction with the results of several other modeling approaches which, either by construction (fixed outer boundaries: e.g., Cook & Royden, 2008; England & Houseman, 1986), or as a result of very week rheology (e.g., Fournier et al., 2004) or of inferred drive by subduction rollback (e.g., Schellart et al., 2019) predict either no Cenozoic extension at all, or large amounts of it where little or none is actually observed.

Be that as it may, despite the overall progress bolstered by the Discrete Element Modeling approach, and notwithstanding the fair agreement between the model's fault growth and slip-line field theory predictions (Figure 5 and Supplementary Animations in Supporting Information S1), significant shortcomings remain in the modeling strategy and in the fit between the model results and first order tectonic observations across western Asia.

First and foremost, by design, the model cannot account for the deformation of impacting India along the indenter front, namely along and near the Himalayan range, south of the Zangbo suture. This is bound to impact the overall deformation rates north of the indenter front during periods of fast Himalayan thrusting in ways that remain to be quantified. Moreover, the potential effect of the curvature of the range in contributing to drive extension across southern Tibet (e.g., Armijo et al., 1986; Baranowski et al., 1984) cannot be assessed.

Also, the model does not integrate superficial erosion or deposition processes, whose role should not be negligible, even though post thickening erosion was restricted by internal drainage across much of the west-central Tibet Plateau (e.g., Liu-Zeng et al., 2008, and References there-in). Additionally, although that is equally the case for most other attempts at modeling the broad-scale deformation of SE Asia, the potential effects of the curvature of the earth are not examined.

Second, perhaps the most noticeable difference between faulting and related deformation in the model and in Asia is the overall orientation of the large sinistral strike-slip faults S1 and S2. They strike mostly 30–40° more northerly than do the ASRR and ATF/HY faults. We surmise that this might be mostly a consequence of the pre-Tertiary geological history. While the impacted continent in the DEM is a mechanically homogeneous medium, Asia is a heterogeneous assemblage of blocks of different ages, accreted at different times. Such age differences must strongly impact their strengths, hence mechanical responses to the stresses generated by the collision (e.g., Cook & Royden, 2008; Molnar & Tapponnier, 1981).

Specifically, Tibet is surrounded to the north, east and southeast by Precambrian blocks (Tarim, North and South China, Kontum) whose strong Archean to Neoproterozoic lithospheres (≈2.8 to 0.8 Ga; e.g., Faure et al., 2007; Jiang et al., 2020; Song et al., 2017; Z. N. Yang et al., 2018; C. L. Zhang et al., 2012; Zhao and Zhai, 2013; and references there-in) likely impede the straightforward propagation of new strike-slip faults. For instance, the ATF, which hugs the southern edge of the Tarim block, striking ≈N75°E for hundreds of kilometers, fails to directly cross Northeast China in that direction. Instead, it bends southwards by ≈40° and converts, across the Qilian Shan, into the Haiyuan Fault, south of the Proterozoic Alxa block (Figure 8). Left-lateral faulting along the ATF/HY system then continues farther eastwards south of the Archean (2.5 Ga) Ordos craton, roughly along the Paleozoic Qinling Shan suture-zone between South and North China (e.g., Mattauer et al., 1985; Peltzer et al., 1985)

(Figure 8). Similarly, the Xianshuihe fault and the ASRR shear zone are strongly deviated southwards, as none of them can easily and straightforwardly cross the Proterozoic (≈0.8 Ga) Yangtze (South China) craton (Figure 8).

Within Tibet, the ≈EW tectonic anisotropy imparted by the pre-Tertiary suturing of the original Paleozoic-Mesozoic Tibetan Terrains, and the correlative ≈NS shortening, hence ≈EW folding (e.g., Meyer et al., 1998 and references there-in), probably also played a role in guiding, at least partially, strike-slip faulting (e.g., Kunlun Fault, southeastern Karakorum fault) (Figure 8).

Clearly, the existence of long, inherited, lithospheric boundaries must account for the significant discrepancies between the orientations of faults in the DE model and in and around Tibet (Figures 8 and 9). Note that the vertical anisotropy serendipitously introduced by plasticine layering in the early, epoch-making analog models of Peltzer and Tapponnier (1988) likely played a mechanical role similar to that of the inherited Asian sutures, accounting in part for their initially remarkable replication of Asian strike-slip faulting.

Lastly, the existence of subducting lithospheric-mantle slabs beneath Tibet remains controversial and, while a few tomographic images are suggestive, the general dearth of seismic events at depths greater than ≈60–80 km beneath the plateau, except in its northwestern-most corner (e.g., Lyon-Caen & Molnar, 1984; Wittlinger et al., 2004) or near the southeastern Zangbo Suture (e.g., De La Torre et al., 2007, and references there-in), makes it difficult to confirm or refute the reality of that process. The lack or scarcity of identifiable intermediate events beneath the plateau may reflect the slowness of potential down-welling rates (≤1 cm/yr), the events small sizes and rarity, the lack of dense enough, dedicated instrumental networks, the insufficient observational time-span, or a combination of all such factors.

Hence, to conclude, it is clear that both more quantitative measurements over broader areas and longer time periods, as well as more advanced modeling strategies, co-involving larger numbers of elements, more complete boundary conditions, and variable, age-dependent model properties, will be needed to make further progress in better understanding the breadth of collision-driven deformation in Asia or elsewhere. But we find it likely that 1/the technical progress in modeling will have to be based on the Discrete Element approach, and 2/the most productive and critical testing ground to better grasp the wealth and subtleties of the deformation of continents will remain southeast Asia, where most of the involved tectonic and related processes occur at unparalleled, fast rates.

Data Availability Statement

I put the code in Zenodo since the paper is interpreted from the numerical results and the code is the only way to reproduce the results. The link to the code composed by me is https://zenodo.org/record/7395343#.Y6W4K-xByOb, and the link to the open-source code is https://yade-dem.org/doc/, which is the platform to compile and execute my code.

Acknowledgments
The modeling results and interpretations presented in this paper are based on a thesis of the PhD work of Liqing Jiao (Earth Observatory of Singapore -EOS-, September 2016). We thank several of our former Singapore colleagues (particularly Prof. Zhenhua Huang, K. Sieh, S. Barbot, Yu Wang, and J. Hubbard) for early discussions, and EOS, for initial funding. Yves Descatoire is thanked for his contribution in drawing Figures 3, 6, 7, 8, and 10b and Figure S8 in Supporting Information S1. Yu Wang kindly provided the broad-scale seismicity data shown in Figure 1. LJ and PT thank both the National Institute of Natural Hazards and the SinoProbe Lab/Institute of Geology, Chinese Academy of Geological Sciences (Beijing, China; CAGS) for the opportunity of pursuing and finishing this research. This project was also partly supported by funding from CAGS (JKY202202). All numerical simulation results can be reproduced using software at this site (https://yade-dem.org/doc/). It includes the source code, installation, documentation, theoretical explanation and examples. The Python code that we developed for the Asian model building, boundary and paramers, other changes (C++ code) we added to YADE (Constitutive Law for Lithospheric deformation and Fault Healing, and Buoyancy function) can be found at https://zenodo.org/record/7395343. Finally, we are grateful to the Editor (P. Tregoning) and Associate Editor (F. Capitanio) and the two referees (one of which, A. Briais) for constructive comments that helped clarify parts of the text and substantially improve some of the figures.

References

Achache, J., Courtillot, V., & Besse, J. (1983). Paleomagnetic constraints on the late Cretaceous and Cenozoic tectonics of southeastern Asia. *Earth and Planetary Science Letters*, *63*(1), 123–136. https://doi.org/10.1016/0012-821x(83)90028-6

Allegre, C. J., Courtillot, V., Tapponnier, P., Hirn, A., Mattauer, M., Coulon, C., et al. (1984). Structure and evolution of the Himalaya–Tibet orogenic belt. *Nature*, *307*(5946), 17–22. https://doi.org/10.1038/307017a0

Allen, C. R., Gillespie, A., Yuan, H., Sieh, K. E., Buchun, Z., & Chengnan, Z. (1984). Red River and associated faults, Yunnan Province, China: Quaternary geology, slip rates, and seismic hazard. *The Geological Society of America Bulletin*, *95*(6), 686–700. https://doi.org/10.1130/0016-7606(1984)95<686:rraafy>2.0.co;2

Armijo, R., Tapponnier, P., & Han, T. (1989). Late Cenozoic right-lateral strike-slip faulting in southern Tibet. *Journal of Geophysical Research*, *94*(B3), 2787–2838. https://doi.org/10.1029/jb094ib03p02787

Armijo, R., Tapponnier, P., Mercier, J., & Han, T. L. (1986). Quaternary extension in southern Tibet: Field observations and tectonic implications. *Journal of Geophysical Research*, *91*(B14), 13803–13872. https://doi.org/10.1029/jb091ib14p13803

Avouac, J. P., & Tapponnier, P. (1993). Kinematic model of active deformation in central Asia. *Geophysical Research Letters*, *20*(10), 895–898. https://doi.org/10.1029/93gl00128

Backhofen, W. A. (1973). Deformation processing. The 1973 Campbell Memorial Lecture The American society for metals.

Baranowski, J., Armbruster, J., Seeber, L., & Molnar, P. (1984). Focal depths and fault plane solutions of earthquakes and active tectonics of the Himalaya. *Journal of Geophysical Research*, *89*(B8), 6918–6928. https://doi.org/10.1029/jb089ib08p06918

Barckhausen, U., & Roeser, H. A. (2004). Seafloor spreading anomalies in the South China Sea revisited. *Continent-ocean interactions within East Asian marginal seas*, *149*, 121–125.

Bradley, K. E., Feng, L., Hill, E. M., Natawidjaja, D., & Sieh, K. (2016). Implications of the diffuse deformation of the Indian Ocean lithosphere for slip partitioning of oblique plate convergence in Sumatra. *Journal of Geophysical Research: Solid Earth*, *122*(1), 572–591. https://doi.org/10.1002/2016jb013549

Briais, A., Patriat, P., & Tapponnier, P. (1993). Updated interpretation of magnetic anomalies and seafloor spreading stages in the South China Sea: Implications for the Tertiary tectonics of Southeast Asia. *Journal of Geophysical Research*, *98*(B4), 6299–6328. https://doi.org/10.1029/92jb02280

Capitanio, F. A., & Replumaz, A. (2013). Subduction and slab breakoff controls on Asian indentation tectonics and Himalayan Western syntaxis formation. *Geochemistry, Geophysics, Geosystems*, *14*(9), 3515–3531. https://doi.org/10.1002/ggge.20171

Chang, C., Chen, N., Coward, M., Deng, W., Dewey, J., Gansser, A., et al. (1986). Preliminary conclusions of the Royal Society and Academia Sinica 1985 geotraverse of Tibet. *Nature*, *323*(6088), 501–507. https://doi.org/10.1038/323501a0

Chang, C., & Zheng, X. (1973). Tectonic features of the Mount Jolmo Lungma region in southern Tibet, China. *Chinese Journal of Geology*, *8*, 1–12.

Chen, L., Capitanio, F. A., Liu, L., & Gerya, T. V. (2017). Crustal rheology controls on the Tibetan plateau formation during India-Asia convergence. *Nature Communications*, *8*(1), 15992. https://doi.org/10.1038/ncomms15992

Chen, Y., Courtillot, V., Cogné, J. P., Besse, J., Yang, Z., & Enkin, R. (1993). The configuration of Asia prior to the collision of India: Cretaceous paleomagnetic constraints. *Journal of Geophysical Research*, *98*(B12), 21927–21941. https://doi.org/10.1029/93jb02075

Cheng, F., Zuza, A. V., Haproff, P. J., Wu, C., Neudorf, C., Chang, H., et al. (2021). Accommodation of India–Asia convergence via strike-slip faulting and block rotation in the Qilian Shan fold–thrust belt, northern margin of the Tibetan Plateau. *Journal of the Geological Society*, *178*(3). https://doi.org/10.1144/jgs2020-207

Chevalier, M. L., Leloup, P. H., Replumaz, A., Pan, J., Métois, M., & Li, H. (2017). Temporally constant slip rate along the Ganzi fault, NW Xianshuihe fault system, eastern Tibet. *The Geological Society of America Bulletin*, *130*(3–4), 396–410. https://doi.org/10.1130/b31691.1

Chevalier, M. L., Pan, J., Li, H., Liu, D., & Wang, M. (2015). Quantification of both normal and right-lateral late Quaternary activity along the Kongur Shan extensional system, Chinese Pamir. *Terra Nova*, *27*(5), 379–391. https://doi.org/10.1111/ter.12170

Chevalier, M. L., Ryerson, F., Tapponnier, P., Finkel, R., Van Der Woerd, J., Haibing, L., & Qing, L. (2005). Slip-rate measurements on the Karakorum fault may imply secular variations in fault motion. *Science*, *307*(5708), 411–414. https://doi.org/10.1126/science.1105466

Chevalier, M. L., Tapponnier, P., Van der Woerd, J., Ryerson, F. J., Finkel, R. C., & Li, H. (2012). Spatially constant slip rate along the southern segment of the Karakorum fault since 200 ka. *Tectonophysics*, *530*, 152–179. https://doi.org/10.1016/j.tecto.2011.12.014

Cobbold, P., & Davy, P. (1988). Indentation tectonics in nature and experiment. 2. Central Asia. *Bulletin of the Geological Institution of the University of Uppsala*, *14*, 143–162.

Cook, K. L., & Royden, L. H. (2008). The role of crustal strength variations in shaping orogenic plateaus, with application to Tibet. *Journal of Geophysical Research*, *113*(B8), 113. https://doi.org/10.1029/2007jb005457

Coudurier-Curveur, A., Tapponnier, P., Okal, E., Van der Woerd, J., Kali, E., Choudhury, S., et al. (2020). A composite rupture model for the great 1950 Assam earthquake across the cusp of the East Himalayan Syntaxis. *Earth and Planetary Science Letters*, *531*, 115928. https://doi.org/10.1016/j.epsl.2019.115928

Craddock, W., Kirby, E., & Zhang, H. (2011). Late Miocene–Pliocene range growth in the interior of the northeastern Tibetan Plateau. *Lithosphere*, *3*(6), 420–438. https://doi.org/10.1130/l159.1

Cundall, P. A., & Strack, O. D. L. (1979). Discrete numerical model for granular assemblies. *Géotechniqu*e, *29*(1), 47–65. https://doi.org/10.1680/geot.1979.29.1.47

Curray, J. R. (2005). Tectonics and history of the Andaman sea region. *Journal of Asian Earth Science*s, 25(1), 187–232. https://doi.org/10.1016/j.jseaes.2004.09.001

Curray, J. R., Moore, D., Lawver, L., Emmel, F., Raitt, R., Henry, M., & Kieckhefer, R. (1979). Tectonics of the Andaman Sea and Burma: Convergentmargins. American Association of Petroleum Geologists, Sperical Volumes A 109, 189-198.

Curray, J. R., & Moore, D. G. (1974). *Sedimentary and tectonic processes in the Bengal deep-sea fan and geosyncline, The geology of continental margins* (pp. 617–627). Springer.

Darman, H. (2017). Seismic Expression of key geological features in The East Natuna basin. *Berita Sedimentologi*, *38*, 50–61.

Davy, P., & Cobbold, P. (1988). Indentation tectonics in nature and experiment. 1. Experiments scaled for gravity. *Bulletin Geological Institution University of Uppsala*, *14*, 129–141.

De la Torre, T., Monsalve, G., Sheehan, A., Sapkota, S., & Wu, F. (2007). Earthquake processes of the Himalayan collision zone in eastern Nepal and the southern Tibetan Plateau. *Geophysical Journal International*, *171*(2), 718–738. https://doi.org/10.1111/j.1365-246x.2007.03537.x

Ding, G., Chen, J., Tian, Q., Shen, X., Xing, C., & Wei, K. (2004). Active faults and magnitudes of left-lateral displacement along the northern margin of the Tibetan Plateau. *Tectonophysics*, *380*(3–4), 243–260. https://doi.org/10.1016/j.tecto.2003.09.022

Donzé, F., Mora, P., & Magnier, S. A. (1994). Numerical simulation of faults and shear zones. *Geophysical Journal International*, *116*(1), 46–52. https://doi.org/10.1111/j.1365-246x.1994.tb02126.x

England, P., & Houseman, G. (1986). Finite strain calculations of continental deformation: 2. Comparison with the India-Asia collision zone. *Journal of Geophysical Research*, *91*(B3), 3664–3676. https://doi.org/10.1029/jb091ib03p03664

England, P., & Molnar, P. (1997). Active deformation of Asia: From kinematics to dynamics. *Science*, *278*(5338), 647–650. https://doi.org/10.1126/science.278.5338.647

Enkin, R., Courtillot, V., Leloup, P., Yang, Z., Xing, L., Zhang, J., & Zhuang, Z. (1992). The paleomagnetic record of uppermost Permian, Lower Triassic rocks from the south China block. *Geophysical Research Letters*, *19*(21), 2147–2150. https://doi.org/10.1029/92gl02321

Fang, X., Dupont-Nivet, G., Wang, C., Song, C., Meng, Q., Zhang, W., et al. (2020). Revised chronology of central Tibet uplift (Lunpola basin). *Science Advances*, *6*(50), eaba7298. https://doi.org/10.1126/sciadv.aba7298

Faure, M., Trap, P., Lin, W., Monié, P., & Bruguier, O. (2007). Polyorogenic evolution of the Paleoproterozoic trans-North China belt, new insights from the in Lüliangshan-Hengshan-Wutaishan and Fuping massifs. *Episodes Journal of International Geoscience*, *30*, 95–106.

Fournier, M., Jolivet, L., Davy, P., & Thomas, J. C. (2004). Backarc extension and collision: An experimental approach to the tectonics of Asia. *Geophysical Journal International*, *157*(2), 871–889. https://doi.org/10.1111/j.1365-246x.2004.02223.x

Gan, W., Zhang, P., Shen, Z. K., Niu, Z., Wang, M., Wan, Y., et al. (2007). Present-day crustal motion within the Tibetan Plateau inferred from GPS measurements. *Journal of Geophysical Research*, *112*(B8), B08416. https://doi.org/10.1029/2005jb004120

Gaudemer, Y., Tapponnier, P., Meyer, B., Peltzer, G., Shunmin, G., Zhitai, C., et al. (1995). Partitioning of crustal slip between linked, active faults in the eastern Qilian Shan, and evidence for a major seismic gap, the 'Tianzhu gap', on the Western Haiyuan Fault, Gansu (China). *Geophysical Journal International*, *120*(3), 599–645. https://doi.org/10.1111/j.1365-246x.1995.tb01842.x

Gaudemer, Y., Tapponnier, P., & Turcotte, D. (1989). River offsets across active strike-slip faults. *Anna. Tecton*, *3*, 55–76.

Gilder, S. A., Coe, R. S., Wu, H., Kuang, G., Zhao, X., Wu, Q., & Tang, X. (1993). Cretaceous and Tertiary paleomagnetic results from southeast China and their tectonic implications. *Earth and Planetary Science Letters*, *117*(3–4), 637–652. https://doi.org/10.1016/0012-821x(93)90108-l

Gilley, L. D., Harrison, T. M., Leloup, P., Ryerson, F., Lovera, O. M., & Wang, J. H. (2003). Direct dating of left-lateral deformation along the Red River shear zone, China and Vietnam. *Journal of Geophysical Research*, *108*(B2). https://doi.org/10.1029/2001jb001726

Griot, D. A., Montagner, J. P., & Tapponnier, P. (1998). Phase velocity structure from Rayleigh and Love waves in Tibet and its neighboring regions. *Journal of Geophysical Research*, *103*(B9), 21215–21232. https://doi.org/10.1029/98jb00953

Hao, M., Wang, Q., Zhang, P., Li, Z., Li, Y., & Zhuang, W. (2020). "Frame wobbling" causing crustal deformation around the Ordos block. *Geophysical Research Letters*, *48*, e2020GL091008. https://doi.org/10.1029/2020GL091008

Harrison, T. M., Leloup, P., Ryerson, F., Tapponnier, P., Lacassin, R., & Chen, W. (1996). Diachronous initiation of transtension along the Ailao Shan-Red River shear zone, Yunnan and Vietnam. *World and Regional Geology*, 208–226.

Houseman, G., & England, P. (1986). Finite strain calculations of continental deformation: 1. Method and general results for convergent zones. *Journal of Geophysical Research*, *91*(B3), 3651–3663. https://doi.org/10.1029/jb091ib03p03651

Huang, K., & Opdyke, N. D. (1992). Paleomagnetism of Cretaceous to lower tertiary rocks from southwestern Sichuan: A revisit. *Earth and Planetary Science Letters*, *112*(1–4), 29–40. https://doi.org/10.1016/0012-821x(92)90004-f

Huang, K., & Opdyke, N. D. (1993). Paleomagnetic results from Cretaceous and Jurassic rocks of South and southwest Yunnan: Evidence for large clockwise rotations in the Indochina and Shan-Thai-Malay terranes. *Earth and Planetary Science Letters*, *117*(3–4), 507–524. https://doi.org/10.1016/0012-821x(93)90100-n

Huang, K., & Opdyke, N. D. (2015). Post-folding magnetization of the Triassic rocks from Western Guizhou and southern Yunnan provinces: New evidence for large clockwise rotations in the Simao terrane. *Earth and Planetary Science Letters*, *423*, 155–163. https://doi.org/10.1016/j.epsl.2015.05.015

Huchon, P., Pichon, X. L., & Rangin, C. (1994). Indochina peninsula and the collision of India and Eurasia. *Geology*, *22*(1), 27–30. https://doi.org/10.1130/0091-7613(1994)022<0027:ipatco>2.3.co;2

Jiang, W., Yu, J.-H., Wang, X., Griffin, W., Pham, T., Nguyen, D., & Wang, F. (2020). Early Paleozoic magmatism in northern Kontum Massif, central Vietnam: Insights into tectonic evolution of the eastern Indochina block. *Lithos*, *376*, 105750. https://doi.org/10.1016/j.lithos.2020.105750

Jiao, L. (2016). *Discrete element modeling of continental deformation and volcanic spine extrusion. Doctoral thesis*. Nanyang Technological University. Retrieved from https://hdl.handle.net/10356/69089

Jiao, L., Chan, C. H., Scholtès, L., Hubert-Ferrari, A., Donzé, F. V., & Tapponnier, P. (2022). Discrete element modeling of a subduction zone with a seafloor irregularity and its impact on the seismic cycle. *Acta Geologica Sinica-English Edition*, *96*(3), 776–790. https://doi.org/10.1111/1755-6724.14935

Jiao, L., Tapponnier, P., Costa, F., Donzé, F.-V., Scholtès, L., Taisne, B., & Wei, S. (2018). Necking and fracking may explain stationary seismicity and full degassing in volcanic silicic spine extrusion. *Earth and Planetary Science Letters*, *503*, 47–57. https://doi.org/10.1016/j.epsl.2018.09.023

Jiao, L., Klinger, Y., & Scholtes, L. (2021). Fault segmentation pattern controlled by thickness of brittle crust. *Geophysical Research Letters*, *48*, e2021GL093390. https://doi.org/10.1029/2021GL093390

Johnson, W., Sowerby, R., & Haddow, J. B. (1970). Plane strain slip-line fields: Theory and bibliography (pp. 62–93). American Elsevier Pub. Co.

Kind, R., Yuan, X., Saul, J., Nelson, D., Sobolev, S., Mechie, J., et al. (2002). Seismic images of crust and upper mantle beneath Tibet: Evidence for Eurasian plate subduction. *Science*, *298*(5596), 1219–1221. https://doi.org/10.1126/science.1078115

Kreemer, C., Blewitt, G., & Klein, E. C. (2014). A geodetic plate motion and Global strain rate model. *Geochemistry, Geophysics, Geosystems*, *15*(10), 3849–3889. https://doi.org/10.1002/2014gc005407

Kusky, T. M., Windley, B., & Zhai, M.-G. (2007). Tectonic evolution of the North China block: From orogen to craton to orogen. *Geological Society, London, Special Publications*, *280*, 1–34. https://doi.org/10.1144/sp280.1

Lacassin, R., Maluski, H., Leloup, P. H., Tapponnier, P., Hinthong, C., Siribhakdi, K., et al. (1997). Tertiary diachronic extrusion and deformation of Western Indochina: Structural and 40Ar/39Ar evidence from NW Thailand. *Journal of Geophysical Research*, *102*(B5), 10013–10037. https://doi.org/10.1029/96jb03831

Lacassin, R., Replumaz, A., & Leloup, P. (1998). Hairpin river loops and slip-sense inversion on southeast Asian strike-slip faults. *Geology*, *26*(8), 703–706. https://doi.org/10.1130/0091-7613(1998)026<0703:hrlass>2.3.co;2

Lacassin, R., Schärer, U., Leloup, P. H., Arnaud, N., Tapponnier, P., Liu, X., & Zhang, L. (1996). Tertiary deformation and metamorphism SE of Tibet: The folded Tiger-leap décollement of NW Yunnan, China. *Tectonics*, *15*(3), 605–622. https://doi.org/10.1029/95tc03749

Lai, K. Y., Chen, Y. G., & Lâm, D. Đ. (2012). Pliocene-to-present morphotectonics of the dien bien Phu fault in northwest Vietnam. *Geomorphology*, *173*, 52–68. https://doi.org/10.1016/j.geomorph.2012.05.026

Lasserre, C., Gaudemer, Y., Tapponnier, P., Mériaux, A. S., Van der Woerd, J., Daoyang, Y., et al. (2002). Fast late Pleistocene slip rate on the Leng long ling segment of the Haiyuan fault, Qinghai, China. *Journal of Geophysical Research*, *107*(B11), ETG 4-1–ETG 4-15. https://doi.org/10.1029/2000jb000060

Lasserre, C., Morel, P. H., Gaudemer, Y., Tapponnier, P., Ryerson, F., King, G., et al. (1999). Postglacial left slip rate and past occurrence of M≥ 8 earthquakes on the Western Haiyuan fault, Gansu, China. *Journal of Geophysical Research*, *104*(B8), 17633–17651. https://doi.org/10.1029/1998jb900082

Le Dain, A. Y., Tapponnier, P., & Molnar, P. (1984). Active faulting and tectonics of Burma and surrounding regions. *Journal of Geophysical Research*, *89*(B1), 453–472. https://doi.org/10.1029/jb089ib01p00453

Leloup, P. H., Arnaud, N., Lacassin, R., Kienast, J., Harrison, T., Trong, T. P., et al. (2001). New constraints on the structure, thermochronology, and timing of the Ailao Shan-Red River shear zone, SE Asia. *Journal of Geophysical Research*, *106*(B4), 6683–6732. https://doi.org/10.1029/2000jb900322

Leloup, P. H., Lacassin, R., Tapponnier, P., Schärer, U., Zhong, D., Liu, X., et al. (1995). The Ailao Shan-Red River shear zone (Yunnan, China), tertiary transform boundary of Indochina. *Tectonophysics*, *251*(1–4), 3–84. https://doi.org/10.1016/0040-1951(95)00070-4

Li, C., Li, J., Ding, W., Franke, D., Yao, Y., Shi, H., et al. (2015). Seismic stratigraphy of the central South China Sea basin and implications for neotectonics. *Journal of Geophysical Research: Solid Earth*, *120*(3), 1377–1399. https://doi.org/10.1002/2014jb011686

Li, H., Chevalier, M., Tapponnier, P., Pan, J., Van der Woerd, J., Mériaux, A., et al. (2021a). Block tectonics across Western Tibet and multi-millennial recurrence of great earthquakes on the Karakax Fault. *Journal of Geophysical Research: Solid Earth*, *126*(12), e2021JB022033. https://doi.org/10.1029/2021jb022033

Li, K., Tapponnier, P., Xu, X., Ren, J., Wang, S., & Zhao, J. (2022a). Holocene slip rate along the Beng Co fault and dextral strike-slip extrusion of central eastern Tibet. *Tectonics*, *41*(8), e2022TC007230. https://doi.org/10.1029/2022tc007230

Li, K., Wang, D., Shao, Q., & Xu, X. (2018). Holocene slip rate along the NE-trending Qixiang Co fault in the central Tibetan plateau and its tectonic implications. *Seismology and Geology*, *40*, 1204. https://doi.org/10.3969/j.issn.0253-4967.2018.06.002

Li, J., Cao, S., Cheng, X., Neubauer, F., Wang, H., & Lv, M. (2022b). Migmatite and leucogranite in a continental-scale exhumed strike-slip shear zone: Implications for tectonic evolution and initiation of shearing. *The Geological Society of America Bulletin*, *134*(3–4), 658–680. https://doi.org/10.1130/b35988.1

Li, S., Advokaat, E. L., van Hinsbergen, D. J., Koymans, M., Deng, C., & Zhu, R. (2017). Paleomagnetic constraints on the Mesozoic-Cenozoic paleolatitudinal and rotational history of Indochina and South China: Review and updated kinematic reconstruction. *Earth-Science Reviews*, *171*, 58–77. https://doi.org/10.1016/j.earscirev.2017.05.007

Li, T., Sun, J., Bao, Y., Zhan, Y., Shen, Z.-K., Xu, X., & Lasserre, C. (2021b). The 2019 Mw 5.8 changning, China earthquake: A cascade rupture of fold-accommodation faults induced by fluid injection. *Tectonophysics*, *801*, 228721. https://doi.org/10.1016/j.tecto.2021.228721

Li, Y., Tian, Y., Yu, C., Su, Z., Jiang, W., Li, Z., et al. (2020). Present-day interseismic deformation characteristics of the Beng Co-Dongqiao conjugate fault system in central Tibet: Implications from InSAR observations. *Geophysical Journal International*, *221*(1), 492–503. https://doi.org/10.1093/gji/ggaa014

Li, Z., Xu, X., Tapponnier, P., Chen, G., Li, K., Luo, J., et al. (2021c). Post-20 ka earthquake scarps along NE-Tibet's Qilian Shan frontal thrust: Multi-millennial Return,∼ characteristic Co-seismic slip, and geological rupture control. *Journal of Geophysical Research: Solid Earth*, *126*(12), e2021JB021889. https://doi.org/10.1029/2021jb02188

Li, Z., Xu, X., Tapponnier, P., Chen, G., Ren, J., Li, K., et al. (2022c). Long, regular Return of four large earthquakes on Qilian Shan's Minle-Damaying frontal thrust (NE Tibet): Partial clustering with great events on the leng long ling fault? *Journal of Geophysical Research: Solid Earth*, *127*(5), e2021JB022800. https://doi.org/10.1029/2021jb022800

Liu, D., Li, H., Sun, Z., Pan, J., Wang, M., Wang, H., & Marie-LuceChevalier (2015). AFT dating constrains the Cenozoic uplift of the Qimen Tagh mountains, Northeast Tibetan plateau, comparison with LA-ICPMS zircon U–Pb ages. *Gondwana Research*, *41*, 438–450. https://doi.org/10.1016/j.gr.2015.10.008

Liu-Zeng, J., Tapponnier, P., Gaudemer, Y., & Ding, L. (2008). Quantifying landscape differences across the Tibetan plateau: Implications for topographic relief evolution. *Journal of Geophysical Research*, *113*(F4), 113. https://doi.org/10.1029/2007jf000897

Long, X., Wilde, S. A., Wang, Q., Yuan, C., Wang, X. C., Li, J., et al. (2015). Partial melting of thickened continental crust in central Tibet: Evidence from geochemistry and geochronology of Eocene adakitic rhyolites in the northern Qiangtang Terrane. *Earth and Planetary Science Letters*, *414*, 30–44. https://doi.org/10.1016/j.epsl.2015.01.007

Lyon-Caen, H., & Molnar, P. (1984). Gravity anomalies and the structure of Western Tibet and the southern Tarim Basin. *Geophysical Research Letters*, *11*(12), 1251–1254. https://doi.org/10.1029/gl011i012p01251

Mansor, M. Y., Rahman, A. H. A., Menier, D., & Pubellier, M. (2014). Structural evolution of Malay basin, its link to Sunda block tectonics. *Marine and Petroleum Geology*, *58*, 736–748. https://doi.org/10.1016/j.marpetgeo.2014.05.003

Mattauer, M., Matte, P., Malavieille, J., Tapponnier, P., Maluski, H., Qin, X. Z., et al. (1985). Tectonics of the Qinling belt: Build-up and evolution of eastern Asia. *Nature*, *317*(6037), 496–500. https://doi.org/10.1038/317496a0

Matte, P., Tapponnier, P., Arnaud, N., Bourjot, L., Avouac, J., Vidal, P., et al. (1996). Tectonics of Western Tibet, between the Tarim and the Indus. *Earth and Planetary Science Letters*, *142*(3–4), 311–330. https://doi.org/10.1016/0012-821x(96)00086-6

Mériaux, A., Ryerson, F., Tapponnier, P., Van der Woerd, J., Finkel, R., Xu, X., et al. (2004). Rapid slip along the central Altyn Tagh Fault: Morphochronologic evidence from Cherchen He and Sulamu Tagh. *Journal of Geophysical Research*, *109*(B6), 109. https://doi.org/10.1029/2003jb002558

Mériaux, A. S., Tapponnier, P., Ryerson, F., Xiwei, X., King, G., Van der Woerd, J., et al. (2005). The Aksay segment of the northern Altyn Tagh fault: Tectonic geomorphology, landscape evolution, and Holocene slip rate. *Journal of Geophysical Research*, *110*(B4). https://doi.org/10.1029/2004jb003210

Mériaux, A. S., Van der Woerd, J., Tapponnier, P., Ryerson, F., Finkel, R., Lasserre, C., & Xu, X. (2012). The Pingding segment of the Altyn Tagh Fault (91°E): Holocene slip-rate determination from cosmogenic radionuclide dating of offset fluvial terraces. *Journal of Geophysical Research*, *117*(B9). https://doi.org/10.1029/2012jb009289

Métivier, F., Gaudemer, Y., Tapponnier, P., & Klein, M. (1999). Mass accumulation rates in Asia during the Cenozoic. *Geophysical Journal International*, *137*(2), 280–318. https://doi.org/10.1046/j.1365-246x.1999.00802.x

Métivier, F., Gaudemer, Y., Tapponnier, P., & Meyer, B. (1998). Northeastward growth of the Tibet plateau deduced from balanced reconstruction of two depositional areas: The Qaidam and Hexi Corridor basins, China. *Tectonics*, *17*(6), 823–842. https://doi.org/10.1029/98tc02764

Meyer, B., Tapponnier, P., Bourjot, L., Métivier, F., Gaudemer, Y., Peltzer, G., et al. (1998). Crustal thickening in Gansu-Qinghai, lithospheric mantle subduction, and oblique, strike-slip controlled growth of the Tibet plateau. *Geophysical Journal International*, *135*, 1–47. https://doi.org/10.1046/j.1365-246x.1998.00567.x

Meyer, B., Tapponnier, P., Gaudemer, Y., Peltzer, G., Shunmin, G., & Zhitai, C. (1996). Rate of left-lateral movement along the easternmost segment of the Altyn Tagh fault, east of 96 E (China). *Geophysical Journal International*, *124*(1), 29–44. https://doi.org/10.1111/j.1365-246x.1996.tb06350.x

Middleton, T. A., Walker, R. T., Rood, D. H., Rhodes, E. J., Parsons, B., Lei, Q., et al. (2016). The tectonics of the Western Ordos plateau, Ningxia, China: Slip rates on the Luoshan and East Helanshan faults. *Tectonics*, *35*(11), 2754–2777. https://doi.org/10.1002/2016tc004230

Molnar, P., Burchfiel, B. C., K'uangyi, L., & Ziyun, Z. (1987). Geomorphic evidence for active faulting in the Altyn Tagh and northern Tibet and qualitative estimates of its contribution to the convergence of India and Eurasia. *Geology*, *15*(3), 249–253. https://doi.org/10.1130/0091-7613(1987)15<249:gefafi>2.0.co;2

Molnar, P., Burchfiel, B. C., Ziyun, Z., K'uangyi, L., Shuji, W., & Minmin, H. (1987). Geologic evolution of northern Tibet: Results of an expedition to Ulugh Muztagh. *Science*, *235*(4786), 299–305. https://doi.org/10.1126/science.235.4786.299

Molnar, P., & Stock, J. M. (2009). Slowing of India's convergence with Eurasia since 20 Ma and its implications for Tibetan mantle dynamics. *Tectonics*, *28*(3). https://doi.org/10.1029/2008tc002271

Molnar, P., & Tapponnier, P. (1981). A possible dependence of tectonic strength on the age of the crust in Asia. *Earth and Planetary Science Letters*, *52*(1), 107–114. https://doi.org/10.1016/0012-821x(81)90213-2

Morley, C. (2012). Late Cretaceous–early Palaeogene tectonic development of SE Asia. *Earth-Science Reviews*, *115*(1–2), 37–75. https://doi.org/10.1016/j.earscirev.2012.08.002

Murphy, M., Sanchez, V., & Taylor, M. (2010). Syncollisional extension along the India–Asia suture zone, south-central Tibet: Implications for crustal deformation of Tibet. *Earth and Planetary Science Letters*, *290*(3–4), 233–243. https://doi.org/10.1016/j.epsl.2009.11.046

Otofuji, Y.-i., Fujihara, M., Tanaka, M., Yokoyama, M., Kitada, K., & Zaman, H. (2012). Tectonic deformation of the southeastern tip of the Indochina Peninsula during its southward displacement in the Cenozoic time. *Gondwana Research*, *22*(2), 615–627. https://doi.org/10.1016/j.gr.2011.09.015

Otofuji, Y.-i., Inoue, Y., Funahara, S., Murata, F., & Zheng, X. (1990). Palaeomagnetic study of eastern Tibet-deformation of the three rivers region. *Geophysical Journal International*, *103*(1), 85–94. https://doi.org/10.1111/j.1365-246x.1990.tb01754.x

Otofuji, Y.-i., Yokoyama, M., Kitada, K., & Zaman, H. (2010). Paleomagnetic versus GPS determined tectonic rotation around eastern Himalayan syntaxis in East Asia. *Journal of Asian Earth Sciences*, *37*(5–6), 438–451. https://doi.org/10.1016/j.jseaes.2009.11.003

Peltzer, G. (1988). *Centrifuged expermiments of continental scale tectonics in Asia* (Vol. 14, pp. 115–128). Bulletin of the Geological Institution of the University of Upsala.
Peltzer, G., & Tapponnier, P. (1988). Formation and evolution of strike-slip faults, rifts, and basins during the India-Asia collision - An experimental approach. *Journal of Geophysical Research-Solid Earth and Planets*, *93*(B12), 15085–15117. https://doi.org/10.1029/jb093ib12p15085
Peltzer, G., Tapponnier, P., & Cobbold, P. R. (1982). Les grands décrochements de l'Est Asiatique: Évolution dans le temps et comparaison avec un modèle expérimental. *Comptes Rendus Geoscience*, *294*, 8.
Peltzer, G., Tapponnier, P., Zhang, Z., & Xu, Z. Q. (1985). Neogene and quaternary faulting in and along the Qinling Shan. *Nature*, *317*(6037), 500–505. https://doi.org/10.1038/317500a0
Plassiard, J. P., Belheine, N., & Donzé, F. V. (2009). A spherical discrete element model: Calibration procedure and incremental response. *Granular Matter*, *11*(5), 293–306. https://doi.org/10.1007/s10035-009-0130-x
Ren, J., Xu, X., Yeats, R. S., & Zhang, S. (2013). Latest Quaternary paleoseismology and slip rates of the Longriba fault zone, eastern Tibet: Implications for fault behavior and strain partitioning. *Tectonics*, *32*(2), 216–238. https://doi.org/10.1002/tect.20029
Replumaz, A., Lacassin, R., Tapponnier, P., & Leloup, P. (2001). Large river offsets and Plio-Quaternary dextral slip rate on the Red River fault (Yunnan, China). *Journal of Geophysical Research: Solid Earth*, *106*(B1), 819–836. https://doi.org/10.1029/2000jb900135
Replumaz, A., & Tapponnier, P. (2003). Reconstruction of the deformed collision zone between India and Asia by backward motion of lithospheric blocks. *Journal of Geophysical Research*, *108*(B6), 108. https://doi.org/10.1029/2001jb000661
Roger, F., Tapponnier, P., Arnaud, N., SchaÈrer, U., Brunel, M., Zhiqin, X., & Jingsui, Y. (2000). An Eocene magmatic belt across central Tibet: Mantle subduction triggered by the Indian collision? *Terra Nova*, *12*(3), 102–108. https://doi.org/10.1046/j.1365-3121.2000.123282.x
Rowley, D. B., & Currie, B. S. (2006). Palaeo-altimetry of the late Eocene to Miocene Lunpola basin, central Tibet. *Nature*, *439*(7077), 677–681. https://doi.org/10.1038/nature04506
Ryerson, F. J., Tapponnier, P., Finkel, R. C., Mériaux, A., Van der Woerd, J., Lasserre, C., et al. (2006). Applications of morphochronology to the active tectomics of Tibet. Geological Society of America Special Paper 415, 61-86.
Schärer, U., Tapponnier, P., Lacassin, R., Leloup, P. H., Dalai, Z., & Shaocheng, J. (1990). Intraplate tectonics in Asia: A precise age for large-scale Miocene movement along the Ailao Shan-Red River shear zone, China. *Earth and Planetary Science Letters*, *97*(1–2), 65–77. https://doi.org/10.1016/0012-821x(90)90099-j
Schärer, U., Xu, R. H., & Allègre, C. J. (1984). UPb geochronology of Gangdese (Transhimalaya) plutonism in the Lhasa-Xigaze region, Tibet. *Earth and Planetary Science Letters*, *69*(2), 311–320. https://doi.org/10.1016/0012-821x(84)90190-0
Schärer, U., Xu, R.-H., & Allègre, C. J. (1986). U (Th) Pb systematics and ages of Himalayan leucogranites, South Tibet. *Earth and Planetary Science Letters*, *77*(1), 35–48. https://doi.org/10.1016/0012-821x(86)90130-5
Schärer, U., Zhang, L. S., & Tapponnier, P. (1994). Duration of strike-slip movements in large shear zones: The Red River belt, China. *Earth and Planetary Science Letters*, *126*(4), 379–397. https://doi.org/10.1016/0012-821x(94)90119-8
Schellart, W., Chen, Z., Strak, V., Duarte, J., & Rosas, F. (2019). Pacific subduction control on Asian continental deformation including Tibetan extension and eastward extrusion tectonics. *Nature Communications*, *10*, 1–15. https://doi.org/10.1038/s41467-019-12337-9
Scholtès, L., & Donzé, F. V. (2013). A DEM model for soft and hard rocks: Role of grain interlocking on strength. *Journal of Mechanics and Physics Solids*, *61*(2), 352–369. https://doi.org/10.1016/j.jmps.2012.10.005
Shi, W., Dong, S., & Hu, J. (2020). Neotectonics around the Ordos block, North China: A review and new insights. *Earth-Science Reviews*, *200*, 102969. https://doi.org/10.1016/j.earscirev.2019.102969
Shi, X., Wang, Y., Sieh, K., Weldon, R., Feng, L., Chan, C. H., & Liu-Zeng, J. (2018). Fault slip and GPS velocities across the Shan Plateau define a curved southwestward crustal motion around the eastern Himalayan syntaxis. *Journal of Geophysical Research: Solid Earth*, *123*(3), 2502–2518. https://doi.org/10.1002/2017jb015206
Sibuet, J. C., Yeh, Y. C., & Lee, C. S. (2016). Geodynamics of the south China sea. *Tectonophysics*, *692*, 98–119. https://doi.org/10.1016/j.tecto.2016.02.022
Šmilauer, V. (2021). *Yade documentation* (3rd ed.). The Yade Project. https://doi.org/10.5281/zenodo.5705394
Socquet, A., Vigny, C., Chamot-Rooke, N., Simons, W., Rangin, C., & Ambrosius, B. (2006). India and Sunda plates motion and deformation along their boundary in Myanmar determined by GPS. *Journal of Geophysical Research*, *111*(B5). https://doi.org/10.1029/2005jb003877
Song, G., Wang, X., Shi, X., & Jiang, G. (2017). New U-Pb age constraints on the upper Banxi Group and synchrony of the Sturtian glaciation in South China. *Geoscience Frontiers*, *8*(5), 1161–1173. https://doi.org/10.1016/j.gsf.2016.11.012
Srisuriyon, K., & Morley, C. (2014). Pull-apart development at overlapping fault tips: Oblique rifting of a Cenozoic continental margin, northern Mergui Basin, Andaman Sea. *Geosphere*, *10*(1), 80–106. https://doi.org/10.1130/ges00926.1
Sternai, P., Avouac, J. P., Jolivet, L., Faccenna, C., Gerya, T., Becker, T. W., & Menant, A. (2016). On the influence of the asthenospheric flow on the tectonics and topography at a collision-subduction transition zones: Comparison with the eastern Tibetan margin. *Journal of Geodynamics*, *100*, 184–197. https://doi.org/10.1016/j.jog.2016.02.009
Sternai, P., Jolivet, L., Menant, A., & Gerya, T. (2014). Driving the upper plate surface deformation by slab rollback and mantle flow. *Earth and Planetary Science Letters*, *405*, 110–118. https://doi.org/10.1016/j.epsl.2014.08.023
Tapponnier, P., Lacassin, R., Leloup, P. H., Schärer, U., Dalai, Z., Haiwei, W., et al. (1990). The Ailao Shan/Red River metamorphic belt: Tertiary left-lateral shear between Indochina and South China. *Nature*, *343*(6257), 431–437. https://doi.org/10.1038/343431a0
Tapponnier, P., Mercier, J., Proust, F., Andrieux, J., Armijo, R., Bassoullet, J., et al. (1981). The Tibetan side of the India–Eurasia collision. *Nature*, *294*(5840), 405–410. https://doi.org/10.1038/294405a0
Tapponnier, P., & Molnar, P. (1976). Slip-line field theory and large-scale continental tectonics. *Nature*, *264*(5584), 319–324. https://doi.org/10.1038/264319a0
Tapponnier, P., & Molnar, P. (1977). Active faulting and tectonics in China. *Journal of Geophysical Research*, *82*(20), 2905–2930. https://doi.org/10.1029/jb082i020p02905
Tapponnier, P., & Molnar, P. (1979). Active faulting and Cenozoic tectonics of the tien Shan, Mongolia, and Baykal regions. *Journal of Geophysical Research*, *84*(B7), 3425–3459. https://doi.org/10.1029/jb084ib07p03425
Tapponnier, P., Peltzer, G., & Armijo, R. (1986). On the mechanics of the collision between India and Asia. *Geological Society, London, Special Publications*, *19*(1), 113–157. https://doi.org/10.1144/gsl.sp.1986.019.01.07
Tapponnier, P., Peltzer, G., Ledain, A. Y., Armijo, R., & Cobbold, P. (1982). Propagating extrusion tectonics in Asia - New insights from simple experiments with plasticine. *Geology*, *10*(12), 611–616. https://doi.org/10.1130/0091-7613(1982)10<611:petian>2.0.co;2
Tapponnier, P., Xu, Z., Roger, F., Meyer, B., Arnaud, N., Wittlinger, G., & Jingsui, Y. (2001). Oblique stepwise rise and growth of the Tibet Plateau. *Science*, *294*(5547), 1671–1677. https://doi.org/10.1126/science.105978

Taylor, M., Yin, A., Ryerson, F. J., Kapp, P., & Ding, L. (2003). Conjugate strike-slip faulting along the Bangong-Nujiang suture zone accommodates coeval east-west extension and north-south shortening in the interior of the Tibetan Plateau. *Tectonics*, *22*(4). https://doi.org/10.1029/2002tc001361

Tian, J., & Lin, Z. (2021). Late Quaternary activity of the Qingchuan Fault, eastern Tibetan Plateau margin: Insights from stream channel offsets and catchment erosion. *Geomorphology*, *395*, 107949. https://doi.org/10.1016/j.geomorph.2021.107949

Tilmann, F., Ni, J., & Team, I. I. S. (2003). Seismic imaging of the downwelling Indian lithosphere beneath central Tibet. *Science*, *300*(5624), 1424–1427. https://doi.org/10.1126/science.1082777

Van Der Woerd, J., Tapponnier, P., Ryerson, J. F., Mériaux, A.-S., Meyer, B., et al. (2002). Uniform postglacial slip-rate along the central 600 km of the Kunlun Fault (Tibet), from 26Al, 10Be, and 14C dating of riser offsets, and climatic origin of the regional morphology. *Geophysical Journal International*, *148*(3), 356–388. https://doi.org/10.1046/j.1365-246x.2002.01556.x

Van Hinsbergen, D. J., Kapp, P., Dupont-Nivet, G., Lippert, P. C., DeCelles, P. G., & Torsvik, T. H. (2011). Restoration of Cenozoic deformation in Asia and the size of greater India. *Tectonics*, *30*(5). https://doi.org/10.1029/2011tc002908

Vassallo, R., Jolivet, M., Ritz, J. F., Braucher, R., Larroque, C., Sue, C., et al. (2007). Uplift age and rates of the Gurvan Bogd system (Gobi-Altay) by apatite fission track analysis. *Earth and Planetary Science Letters*, *259*(3–4), 333–346. https://doi.org/10.1016/j.epsl.2007.04.047

Vilotte, J. P., Daignieres, M., & Madariaga, R. (1982). Numerical modeling of intraplate deformation: Simple mechanical models of continental collision. *Journal of Geophysical Research*, *87*(B13), 10709–10728. https://doi.org/10.1029/jb087ib13p10709

Vilotte, J. P., Daignieres, M., Madariaga, R., & Zienkiewicz, O. (1984). The role of a heterogeneous inclusion during continental collision. *Physics of the Earth and Planetary Interiors*, *36*(3–4), 236–259. https://doi.org/10.1016/0031-9201(84)90049-9

Vilotte, J. P., Madariaga, R., Daignieres, M., & Zienkiewicz, O. (1986). Numerical study of continental collision: Influence of buoyancy forces and an initial stiff inclusion. *Geophysical Journal International*, *84*(2), 279–310. https://doi.org/10.1111/j.1365-246x.1986.tb04357.x

Wang, D., Chang, H., Yin, G., Han, F., Mao, Z., Du, J., et al. (2021). Spatial changes in late Quaternary slip rates along the Gyaring Co Fault: Implications for strain partitioning and deformation modes in Central Tibet. *Tectonics*, *40*(5), e2020TC006110. https://doi.org/10.1029/2020tc006110

Wang, H., Li, K., Chen, L., Chen, X., & Li, A. (2020). Evidence for Holocene activity on the Jiali fault, an active block boundary in the Southeastern Tibetan Plateau. *Seismological Research Letters*, *91*(3), 1776–1780. https://doi.org/10.1785/0220190371

Wang, M., & Shen, Z. K. (2019). Present-day crustal deformation of continental China derived from GPS and its tectonic implications. *Journal of Geophysical Research: Solid Earth*, *125*(2), e2019JB018774. https://doi.org/10.1029/2019jb018774

Wang, W., Qiao, X., Yang, S., & Wang, D. (2017). Present-day velocity field and block kinematics of Tibetan Plateau from GPS measurements. *Geophysical Journal International*, *208*(2), 1088–1102. https://doi.org/10.1093/gji/ggw445

Wang, W. R., Zhao, Y., Liu, X., Hu, J., Wei, C., Xiao, W., et al. (2019). Metamorphism of diverse basement gneisses of the Ordos Basin: Record of multistage Paleoproterozoic orogenesis and constraints on the evolution of the Western North China Craton. *Precambrian Research*, *328*, 48–63. https://doi.org/10.1016/j.precamres.2019.03.012

Wang, Y., Sieh, K., Tun, S. T., Lai, K. Y., & Myint, T. (2014). Active tectonics and earthquake potential of the Myanmar region. *Journal of Geophysical Research: Solid Earth*, *119*(4), 3767–3822. https://doi.org/10.1002/2013jb010762

Watkinson, I., Elders, C., Batt, G., Jourdan, F., Hall, R., & McNaughton, N. J. (2011). The timing of strike-slip shear along the Ranong and Khlong Marui faults, Thailand. *Journal of Geophysical Research*, *116*(B9), B09403. https://doi.org/10.1029/2011jb008379

Wittlinger, G., Tapponnier, P., Poupinet, G., Mei, J., Danian, S., Herquel, G., & Masson, F. (1998). Tomographic evidence for localized lithospheric shear along the Altyn Tagh fault. *Science*, *282*(5386), 74–76. https://doi.org/10.1126/science.282.5386.74

Wittlinger, G., Vergne, J., Tapponnier, P., Farra, V., Poupinet, G., Jiang, M., et al. (2004). Teleseismic imaging of subducting lithosphere and Moho offsets beneath Western Tibet. *Earth and Planetary Science Letters*, *221*(1–4), 117–130. https://doi.org/10.1016/s0012-821x(03)00723-4

Wu, C., Li, H., Leloup, P. H., Yu, C., Si, J., Liu, D., et al. (2014). High-angle fault responsible for the surface ruptures along the northern segment of the Wenchuan Earthquake Fault Zone: Evidence from the latest seismic reflection profiles. *Tectonophysics*, *619*, 159–170. https://doi.org/10.1016/j.tecto.2013.09.015

Wu, F. T., & Wang, P. (1988). Tectonics of Western Yunnan province, China. *Geology*, *16*(2), 153–157. https://doi.org/10.1130/0091-7613(1988)016<0153:towypc>2.3.co;2

Wu, Z., Shentu, B. Cao, Z., & Deng, Q. (1990). The surface ruptures of Danxung (Tibet) earthquake (M= 8) in 1411. *Seismology and Geology*, *12*, 98–108.

Xu, X., Wen, X., Yu, G., Chen, G., Klinger, Y., Hubbard, J., & Shaw, J. (2009). Coseismic reverse-and oblique-slip surface faulting generated by the 2008 Mw 7.9 Wenchuan earthquake, China. *Geology*, *37*(6), 515–518. https://doi.org/10.1130/g25462a.1

Yamashita, I., Surinkum, A., Wada, Y., Fujihara, M., Yokoyama, M., Zaman, H., & Otofuji, Y.-i. (2011). Paleomagnetism of the middle–late Jurassic to Cretaceous red beds from the peninsular Thailand: Implications for collision tectonics. *Journal of Asian Earth Sciences*, *40*(3), 784–796. https://doi.org/10.1016/j.jseaes.2010.11.001

Yang, Z., & Besse, J. (1993). Paleomagnetic study of Permian and Mesozoic sedimentary rocks from Northern Thailand supports the extrusion model for Indochina. *Earth and Planetary Science Letters*, *117*(3–4), 525–552. https://doi.org/10.1016/0012-821x(93)90101-e

Yang, Z., & Besse, J. (2001). New Mesozoic apparent polar wander path for South China: Tectonic consequences. *Journal of Geophysical Research*, *106*(B5), 8493–8520. https://doi.org/10.1029/2000jb900338

Yang, Z., Besse, J., Sutheetorn, V., Bassoullet, J., Fontaine, H., & Buffetaut, E. (1995). Lower-Middle Jurassic paleomagnetic data from the Mae Sot area (Thailand): Paleogeographic evolution and deformation history of Southeastern Asia. *Earth and Planetary Science Letters*, *136*(3–4), 325–341. https://doi.org/10.1016/0012-821x(95)00192-f

Yang, Z., Yin, J., Sun, Z., Otofuji, Y., & Sato, K. (2001). Discrepant Cretaceous paleomagnetic poles between eastern China and Indochina: A consequence of the extrusion of Indochina. *Tectonophysics*, *334*(2), 101–113. https://doi.org/10.1016/s0040-1951(01)00061-0

Yang, Z. N., Yang, K. G., Polat, A., & Xu, Y. (2018). Early crustal evolution of the eastern Yangtze Block: Evidence from detrital zircon U-Pb ages and Hf isotopic composition of the Neoproterozoic Huashan Group in the Dahongshan area. *Precambrian Research*, *309*, 248–270. https://doi.org/10.1016/j.precamres.2017.05.011

Yin, A., & Harrison, T. M. (2000). Geologic evolution of the Himalayan-Tibetan orogen. *Annual Review of Earth and Planetary Sciences*, *28*(1), 211–280. https://doi.org/10.1146/annurev.earth.28.1.211

Yin, A., Harrison, T. M., Ryerson, F., Wenji, C., Kidd, W., & Copeland, P. (1994). Tertiary structural evolution of the Gangdese thrust system, southeastern Tibet. *Journal of Geophysical Research*, *99*(B9), 18175–18201. https://doi.org/10.1029/94jb00504

Yuan, D. Y., Champagnac, J. D., Ge, W. P., Molnar, P., Zhang, P. Z., Zheng, W. J., et al. (2011). Late Quaternary right-lateral slip rates of faults adjacent to the lake Qinghai, northeastern margin of the Tibetan Plateau. *The Geological Society of America Bulletin*, *123*(9–10), 2016–2030. https://doi.org/10.1130/b30315.1

Zhang, C. L., Li, H. K., Santosh, M., Li, Z. X., Zou, H. B., Wang, H., & Ye, H. (2012). Precambrian evolution and cratonization of the Tarim Block, NW China: Petrology, geochemistry, Nd-isotopes and U–Pb zircon geochronology from Archaean gabbro-TTG–potassic granite suite and Paleoproterozoic metamorphic belt. *Journal of Asian Earth Sciences*, *47*, 5–20. https://doi.org/10.1016/j.jseaes.2011.05.018

Zhang, Y. G., Zheng, W. J., Wang, Y. J., Zhang, D. L., Tian, Y. T., Wang, M., et al. (2018). Contemporary deformation of the North China plain from Global positioning system data. *Geophysical Research Letters*, *45*(4), 1851–1859. https://doi.org/10.1002/2017gl076599

Zhang, Y. Q., Chen, Z. L., & Yang, N. (2001). New geological evidence for late Cenozoic left-lateral displacement along the Altyn Tagh Fault. *Geoscience*, *15*, 8–12.

Zhang, Y. Q., Mercier, J. L., & Vergély, P. (1998). Extension in the graben systems around the Ordos (China), and its contribution to the extrusion tectonics of south China with respect to Gobi-Mongolia. *Tectonophysics*, *285*(1–2), 41–75. https://doi.org/10.1016/s0040-1951(97)00170-4

Zhao, G., & Zhai, M. (2013). Lithotectonic elements of Precambrian basement in the North China craton: Review and tectonic implications. *Gondwana Research*, *23*(4), 1207–1240. https://doi.org/10.1016/j.gr.2012.08.016

Zheng, W. J., Zhang, P. Z., He, W. G., Yuan, D. Y., Shao, Y. X., Zheng, D. W., et al. (2013). Transformation of displacement between strike-slip and crustal shortening in the northern margin of the Tibetan Plateau: Evidence from decadal GPS measurements and late Quaternary slip rates on faults. *Tectonophysics*, *584*, 267–280. https://doi.org/10.1016/j.tecto.2012.01.006

Zuza, A. V., Cheng, X., & Yin, A. (2016). Testing models of Tibetan Plateau formation with Cenozoic shortening estimates across the Qilian Shan–Nan Shan thrust belt. *Geosphere*, *12*(2), 501–532. https://doi.org/10.1130/ges01254.1

Zuza, A. V., Wu, C., Reith, R. C., Yin, A., Li, J., Zhang, J., et al. (2018). Tectonic evolution of the Qilian Shan: An early Paleozoic orogen reactivated in the Cenozoic. *The Geological Society of America Bulletin*, *130*(5–6), 881–925. https://doi.org/10.1130/b31721.1